

# HLPW-4/GMGW-3: Mesh Adaptation for RANS Technology

## Focus Group Workshop Summary

Michael A. Park\*

*NASA Langley Research Center, Hampton, VA 23681, USA*

Frédéric Alauzet<sup>†</sup>

*INRIA Paris-Saclay, Alan Turing Building, 91120 Palaiseau, France*

Todd Michal<sup>‡</sup>

*Boeing Research & Technology, St. Louis, MO 63166, USA*

The AIAA workshop series helps guide the Computational Fluid Dynamics (CFD) community through publicly available test cases and impartial evaluation to establish the state-of-the-art in applied CFD. A summary of the Mesh Adaptation Technical Focus Group submissions for the joint Fourth CFD High Lift Prediction and Third Geometry & Mesh Generation Workshop is provided. The Common Research Model High-Lift variant (CRM-HL) is the target of this investigation. A 2D high-lift airfoil solution verification case was extracted from the 3D CRM-HL. Low variation is shown between 2D solutions with mesh adaptation to control estimated solution interpolation and output errors. As expected, variation for these mesh adaptation techniques is larger for the 3D CRM-HL than the 2D airfoil. More importantly, the 3D mesh adapted results have a lower variation than expert-crafted meshes of equal or larger size. Suspected multiple solutions to Reynolds-averaged Navier-Stokes with the Spalart-Allmaras turbulence model appear to resolve into a common solution with mesh resolution.

### I. Introduction

A multielement wing with leading edge and trailing edge devices is typically employed in high-lift aerodynamic design. The interaction of these elements impact the pressure distributions and boundary layers of the high-lift system elements [1]. Rumsey and Ying [2] depict the complex features that emerge from the interaction of these devices. There is high streamline curvature and steep favorable and adverse pressure gradients. With low-Mach free stream conditions, the fluid accelerates from incompressible to near sonic or low supersonic compressible conditions. Vortical flow is produced by attachment hardware, vortex generators, and the ends of slat and flap segments. Each wing element (e.g., slat, main wing, flap) has a boundary layer that progresses through stagnation, laminar flow, transitional flow, and developed turbulent flow. The intersection of nacelle, pylon, wing elements, and attachment hardware create corner flows. Wakes are generated by wing elements and attachment hardware. These wakes merge with boundary layers to influence local boundary layer state and boundary layer separation. Cove regions are required to transform the multiple elements into a cruise wing shape. These cove regions create recirculation. The complex interaction of these features gives rise to unsteady flow.

The challenges in applying Computational Fluid Dynamics (CFD) to high-lift flows are listed by Clark et al. [3]. The ground testing and simulation research community is organizing to address these challenges. The CFD 2030 Vision Study [4] identifies related limitations in current CFD practice and establishes a roadmap to motivate continued investment in technologies to address these limitations. Some of the vision implementation challenges include leveraging rapidly evolving high-performance computer hardware, inherent turbulence modeling limitations in Reynolds-averaged Navier-Stokes (RANS) CFD methods, developing practical methods to resolve turbulence with large-eddy simulation (LES), and addressing bottlenecks in geometry, mesh generation, and adaptivity workflows. A critical low-speed (high-lift) maneuver typically performed for airplane certification is a grand challenge identified to energize the aerospace CFD and aerodynamics communities by coordinating and collaborating across multiple levels of government, industry,

---

\*Research Scientist, Computational AeroSciences Branch, AIAA Associate Fellow.

<sup>†</sup>Senior Researcher, GAMMA Team, AIAA Associate Fellow.

<sup>‡</sup>Retired, AIAA Associate Fellow.

academia, and other technology providers to accelerate the use of efficient and robust computational tools [5]. Maximum lift and stall prediction is a case study in the 20-year vision for virtual flight and engine testing to provide a Guide for Aircraft Certification by Analysis (CbA) [6], which includes a roadmap where many applications and predictive capabilities are influenced by the success of high-lift prediction and continuation of CFD verification exercises.

To advance the state of the art in predicting high-lift flows, an open international workshop series was established with long-term objectives [7].

- 1) Assess the numerical prediction capability (mesh, numerics, turbulence modeling, high-performance computing requirements, etc.) of current-generation CFD technology for swept, medium/high-aspect ratio wings in landing/takeoff (high-lift) configurations
- 2) Develop practical modeling guidelines for CFD prediction of high-lift flow fields
- 3) Advance the understanding of high-lift flow physics to enable development of more accurate prediction methods and tools
- 4) Determine the elements of high-lift flow physics that are critical for modeling to enable the development of more accurate prediction methods and tools
- 5) Enhance CFD prediction capability for practical high-lift aerodynamic design and optimization

Three previous High Lift Prediction Workshops have been held to further these objectives. The First High Lift Prediction Workshop (HLPW-1) [8, 9] studied the NASA Trapezoidal Wing configuration [10, 11]. The Second High Lift Prediction Workshop (HLPW-2) [12] studied the DLR-F11 configuration [13]. HLPW-2 included a turbulence modeling verification exercise to understand the differences in turbulence model implementation between participant codes. HLPW-3 [14] studied both a simplified version of the Common Research Model High-Lift variant (CRM-HL) [15] and the JAXA Standard Model [16]. HLPW-3 was held in partnership with the First Geometry and Mesh Generation Workshop (GMGW-1) [17]. This HLPW-3 and GMGW-1 partnership is critical to supporting geometry processing and mesh generation for complex high-lift configurations with detailed slat and flap attachment hardware. The Second Geometry and Mesh Generation Workshop (GMGW-2) [18] included cases on generating an extremely fine mesh and a uniformly refined mesh family for the simplified version of CRM-HL.

The Fourth High Lift Prediction Workshop (HLPW-4) was held concurrently with the Third Geometry and Mesh Generation Workshop (GMGW-3). HLPW-4 is organized differently than previous AIAA prediction workshops, which employed multiple small participant groups organized by their host institution [7]. HLPW-4 is organized into a small number of Technical Focus Groups (TFG) composed of members with both active participant and observer roles.

- 1) Geometry Modeling and Preparation for Meshing (GEOM)
- 2) Fixed Grid RANS (RANS)
- 3) Mesh Adaptation for RANS (ADAPT)
- 4) High Order Discretization (HO)
- 5) Hybrid RANS/LES (HRLES)
- 6) Wall-Modeled LES and Lattice-Boltzmann (WMLESLB)

The article summarizes the findings of ADAPT TFG. The CRM-HL with flow-through nacelle and slat/flap support hardware [19] is the shared test case for all TFGs. A wind tunnel test was conducted in preparation for the workshop [20], which defines the flap angles, flap gaps, flap overlaps, slat height, and slat gap used in HLPW-4. A three-element high-lift airfoil derived from the CRM-HL is also provided for turbulence model verification.

The primary focus of ADAPT is the verification of solution-based mesh adaptation methods and flow solvers for the Spalart-Allmaras (SA) [21] turbulence model. SA (or its negative variant SA-neg [22]) is used exclusively in the ADAPT TFG without corrections because consistency of implementation is easier to establish for SA than SA with correction terms. The formal validation of the SA model with experimental measurements is not in the scope of ADAPT. Significant modeling errors between RANS-SA and the experiment are expected, particularly near and above maximum lift conditions. The goal of ADAPT is to provide consistent and reliable solutions to the RANS-SA equations. However, experimental measurements will be presented with simulations to provide context for the utility of these simulations. Differences between RANS-SA solutions and the experimental measurements are shown to provide evidence of modeling error with controlled discretization error (and controlled iterative error in many submissions). A more complete understanding of modeling error defines the utility of these methods as applied to high-lift predictions and may support continued development of RANS turbulence models.

Wing root side of body separation in the Drag Prediction Workshop (DPW) series provides a case study in how mesh effects can commingle with modeling approximations to complicate the comparison to experimental measurements for the high-speed CRM [23]. CFD solutions that differ from experiment measurements are also observed in the HLPW series. The DPW-5 summary [24] noted, "Some solutions exhibited a large side of body separation bubble

that was not observed in the wind-tunnel results." In a review of DPW-4 participant results [25], modeling the full Navier-Stokes viscous terms had a larger bubble size than thin-layer Navier-Stokes and increasing the wing-root juncture mesh resolution increased the extent of separation. Efforts to use finer meshes and fewer approximations increased the differences between CFD and experiment. Yamamoto, Tanaka, and Murayama [26] showed that QCR (Quadratic Constitutive Relationship) [27] decreased the extent of the side of body separation and reduced the differences between CFD and experiment. QCR replaces the linear stress-strain Boussinesq relationship and changes the modeling of turbulent stresses. The trend of SA-QCR decreasing the extent of the side of body separation over SA was confirmed in DPW-5 [28, 29]. Before the identification of the connection between QCR and side of body separation extent, CFD simulations showing large side of body separation extent were considered outliers. Participants are motivated to avoid the outlier label in these workshop settings and this stigma may have inhibited the understanding of modeling effects or delayed the application of QCR in DPW-2 [30] or DPW-3 [31]. In the context of HLPW-4, the understanding of modeling effects can be enhanced by showing differences between the topology of CFD skin friction contours and experimental oil flow images, especially if mesh effects can be quantified and reduced.

Each of the technology focus groups were tasked with creating a list of key questions to be studied and addressed in HLPW-4. Before listing the ADAPT key questions, the nomenclature used in these ADAPT key questions is defined. **Multiple solutions** are converged CFD solutions, which are dependent on initial conditions [32]. A coarse mesh, initial conditions, and incomplete iterative convergence can complicate the identification of multiple solutions. A **metric field** is an anisotropic specification of mesh resolution used to adapt the mesh. **Complexity** is a measure of a metric that can provide a sharp estimate of the adapted mesh size (number of vertices or number of elements) [33, 34]. **Complexity continuation** is holding the angle of attack fixed to create a series of adapted meshes with increasing complexity. This is the continuous analog to a mesh convergence study [33, 34]. Multiple **subiterations** are performed at a fixed complexity before complexity is increased to perform complexity continuation. **Angle of attack continuation** is holding the complexity or the mesh fixed and increasing angle of attack [35]. Angle of attack continuation can encourage a particular solution from multiple possible solutions. Complexity continuation allows all angles of attack to be computed independently for an angle of attack range. Angle of attack continuation can reduce throughput of angle of attack sweeps by requiring simulations to be completed at lower angle of attack before proceeding to higher angles of attack. The **multiscale metric** is an anisotropic specification of mesh resolution to control estimated interpolation error in a scalar field, which is typically Mach number [36, 37]. A **goal-oriented metric** is a method to control estimated error in an output (e.g., lift, drag) [38, 39]. The ADAPT key questions are listed here and revisited in Section IX. The sections that support each key question are listed after each question.

- 1) Can adaptive mesh convergence be achieved on the CRM-HL model across the angle of attack range? (Sections III, IV, and V)
- 2) What are the best practices, lessons learned, and outstanding technical issues for adaptive mesh modeling of high-lift applications (e.g., error estimate choice, flow solver settings, complexity schedule, solution continuation, geometry handling)? (Section VI)
- 3) Can the causes of multiple solutions and techniques to encourage the "desired" branch be identified (e.g., incomplete iterative convergence, discretization error, initial conditions, solver settings)? (Section VII)
- 4) Where can mesh adapted RANS contribute to prediction of high-lift flow physics? (Section VIII)

These questions were reorganized in the months leading up to the workshop to simplify and make these questions more orthogonal to each other.

The components of unstructured mesh adaptation are shown in Fig. 1. Starting with an initial mesh, a primal flow solution is computed, followed optionally by an adjoint solution for a goal-oriented metric. The adjoint corresponds to a particular output quantity (e.g., lift, drag). The information from the flow (and adjoint) solution is used to estimate error and specify a new mesh resolution and orientation request via a Riemannian metric field. The current mesh system is modified by mesh mechanics to adhere to the metric. Once the adapted mesh is available, the previous flow solution is interpolated on the new mesh to provide an initial condition that approximates the steady-state solution on that adapted mesh. The process is repeated until exit criteria are met (e.g., accuracy requirement, resource limit).

The status of unstructured mesh adaptation techniques was documented in the years 2015 [40] and 2016 [41]. Recommended investments from these reviews are underway. For example, verification exercises for analytic functions [42], a wing in transonic flow [43], and a multielement airfoil [44] have been completed. These verification exercises utilized multiscale and goal-based metrics [39, 45–47]. These verified mesh adaptation methods have been applied to HLPW-3 [48] and HLPW-3 configurations after the workshop [35, 49–52].

These recommended investments in unstructured mesh adaptation technology include parallel execution for the large mesh sizes [53] required for complex simulations like the CRM-HL. Mechanical Computer Aided Design (MCAD) [54]

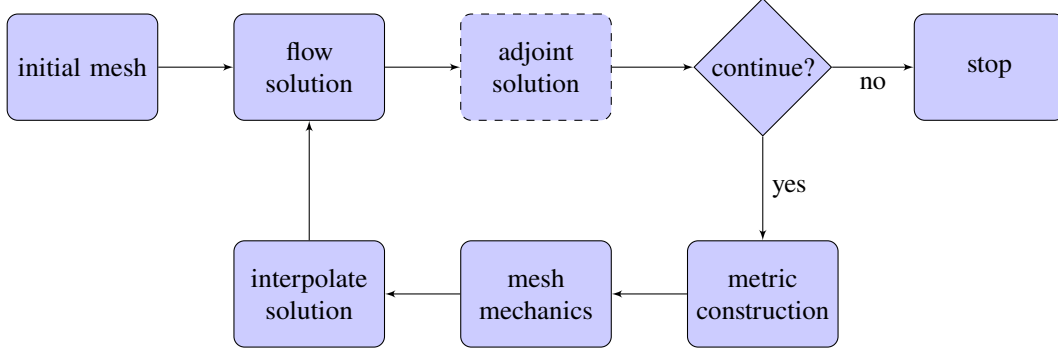


**Fig. 1 Solution-based mesh adaptation process.**

geometry sources must be accepted with boundary representation tolerances that are looser than HLPW-4 meshing guides and adaptive mesh requirements [55]. Investments in geometry accommodation are critical to participation in HLPW-4, because interpretations of the wind tunnel MCAD into a solid model for analysis in the workshop contain complex topology at typical boundary representation tolerances [56].

The members of the ADAPT TFG used these unstructured mesh adaptation investments to address the key questions and a summary of this effort is provided in the following sections. A multielement airfoil extracted from the CRM-HL is used to verify the solution-based mesh adaptation. Mesh convergence is shown for the 3D CRM-HL at  $7.05^\circ$  angle of attack. Angle of attack ranges are computed to and beyond maximum lift. Best practices are identified for mesh adaptation application. The impact of mesh refinement on suspected multiple solutions is identified. The contributions of mesh adaptation techniques to high-lift prediction are distilled. Recommendations for continued investments are extracted.

## II. Submissions

The submissions are listed in Table 1. The participant identifier is established by the HLPW-4 committee with an integer suffix added to create the submission identifier in the case of multiple submissions. The workshop established a convention of marking a submission as “best practice”. The A-013.1 submission in Table 1 with a footnote is not marked with best practice and is produced from an expert-crafted mesh series. The teams producing these submissions are composed of multiple members and the corresponding member is listed. The solver, mesher, and metric triplets are described in the following paragraphs.

**Table 1 ADAPT TFG Submissions.**

Submission	Solver	Mesher	Metric	Organization	Contact
A-002	WOLF	FEFLO.A	Lift	INRIA	F. Alauzet
A-004.1	FUN3D-FV	REFINE	Multiscale	NASA	M. Park
A-004.2	FUN3D-SFE	REFINE	Multiscale	NASA	M. Park
A-013.1 <sup>1</sup>	SANS	TMR	Expert	MIT	M. Galbraith
A-013.2	SANS	EPIC	Drag	MIT	M. Galbraith
A-025.1	GGNS	EPIC	Multiscale	Boeing	B. Ahrabi
A-025.2	GGNS	EPIC	Drag	Boeing	B. Ahrabi
A-026	HEMLAB	PYAMG	Multiscale	ITU	M. Sahin
A-031	COFFE	REFINE	Multiscale	UT	K. Holst

<sup>1</sup> Expert-crafted, not labeled “best practice”

The WOLF flow solver is vertex-centered combination of finite-volume convective terms and finite-element viscous terms [37, 57]. The FUN3D (Fully-Unstructured Navier-Stokes 3D) framework [58] contains finite-volume FUN3D-



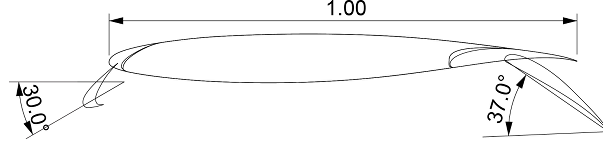
FV [59] and stabilized finite-element FUN3D-SFE [60] formulations. GGNS (General Geometry Navier-Stokes) is a Streamline upwind Petrov–Galerkin finite-element discretization [32]. HEMLAB is a vertex-centered hybrid finite-volume solver [61]. SANS (Solution Adaptive Numerical Simulator) is a general framework for solving discrete finite-element approximations [62]. COFFE (Conservative Field Finite Element) [63, 64] is a stabilized finite-element method. The finite-element solvers used a linear (P1) basis in the ADAPT TFG. Submissions with higher-order solution approximations are documented in the HO TFG [65].

FEFLO.A uses generalized operators based on recasting the standard split, collapse, and swap operators in a cavity framework [66, 67]. PYAMG uses an algorithm similar to FEFLO.A [68]. REFINE uses classic split, collapse, and element swap operations in a distributed-memory parallel environment [69] with cavity operators [66] to recover the surface. FEFLO.A and REFINE use Engineering Geometry Aircraft Design System (EGADS) [70, 71] to query geometry such as the CRM-HL MCAD solid. EPIC (Edge Primitive Insertion and Collapse) uses classic mesh operations in a parallel execution scheme [72].

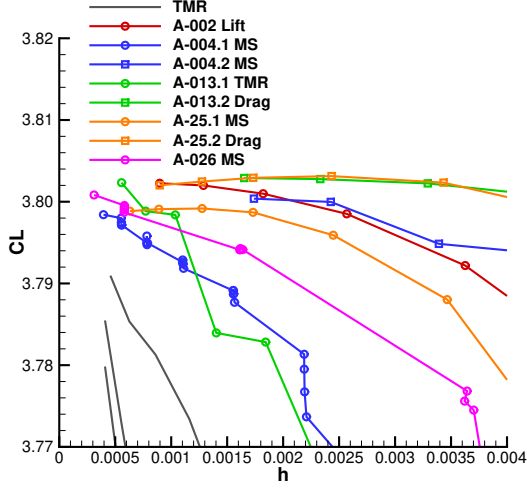
The multiscale metric controls the  $L^p$  norm of the interpolation error of a solution scalar field and forms the foundation of some output-based metrics [33, 37]. The multiscale metric implementations have been verified before the workshop [42–44]. The submission A-002 lift-based metric is described by Alauzet and Frazza [46]. The submission A-013.2 drag-based metric is described by Carson et al. [73]. The submission A-025.2 drag-based metric is described by Kamenetskiy et al. [47]. Submission A-013.1 uses a mesh from the TMR (Turbulence Modeling Resource) [74, 75].

### III. Airfoil Verification Case

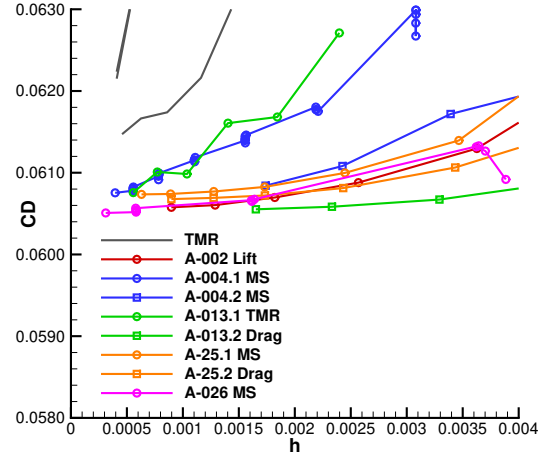
The 2D CRM-HL airfoil has become a popular multielement airfoil verification case across the angle of attack range [44, 76–81]. The target conditions for HLPW-4 are standard sea-level conditions with Mach number of 0.2, Reynolds number of 5M based on the reference chord, and  $16^\circ$  angle of attack. All flow solutions were computed with the SA turbulence model. The airfoil is shown in Fig. 2a. Lift coefficient is shown in Fig. 2b and the drag coefficient is shown in Fig. 2c. The characteristic length  $h$  in these figures is computed as  $h = N^{-1/2}$  where  $N$  is the number of degrees of freedom (vertices for these discretizations) for this 2D case. The gray lines without symbols labeled TMR are the results using uniformly-refined expert-crafted meshes. The adapted-mesh results approach the range of  $C_L = [3.799, 3.802]$  and  $C_D = [0.0605, 0.0607]$ . The results based on TMR meshes are approaching at a steep slope and it is unclear if these TMR mesh results will reach the range indicated by the adapted mesh with additional mesh refinement. Goal-oriented methods converge more rapidly to fine-mesh forces than multiscale and approach fine-mesh results with a smaller slope.



(a) Geometry and rigging.



(b) Lift coefficient.



(c) Drag coefficient.

Fig. 2 Grid convergence of the 2D CRM-HL airfoil SA verification case.

#### IV. Mesh Convergence

Convergence of best practice submissions for the 3D CRM-HL at  $7.05^\circ$  angle of attack is shown in Fig. 3. The free stream conditions are 0.2 Mach, 5.49M Reynolds number based on mean aerodynamic chord, and  $521^\circ\text{R}$ . The characteristic length  $h$  in these figures is computed as  $h = N^{-1/3}$  where  $N$  is the number of degrees of freedom (vertices for these discretizations) for this 3D case. See Section VIII for these ADAPT submissions in context of the other TFG results. The range of the vertical axis is very small in these figures, which exaggerates the differences between submissions. When the ADAPT submissions are placed in context of other TFG results, a wider scale is used and the ADAPT submissions appear more congruent, see Section VIII. The lift coefficient is shown in Fig. 3a. The variation between submissions decreases with smaller  $h$  and the trend is toward higher lift with finer mesh spacing. The drag coefficient is shown in Fig. 3b. While variation in drag coefficient is decreasing with mesh refinement, the trajectories of each submission appear more distinct than lift and pitching moment mesh refinement trajectories. The pitching moment coefficient is shown in Fig. 3c. The variation between submissions decreases with smaller  $h$  and the trend is for more negative pitching moment with mesh refinement.

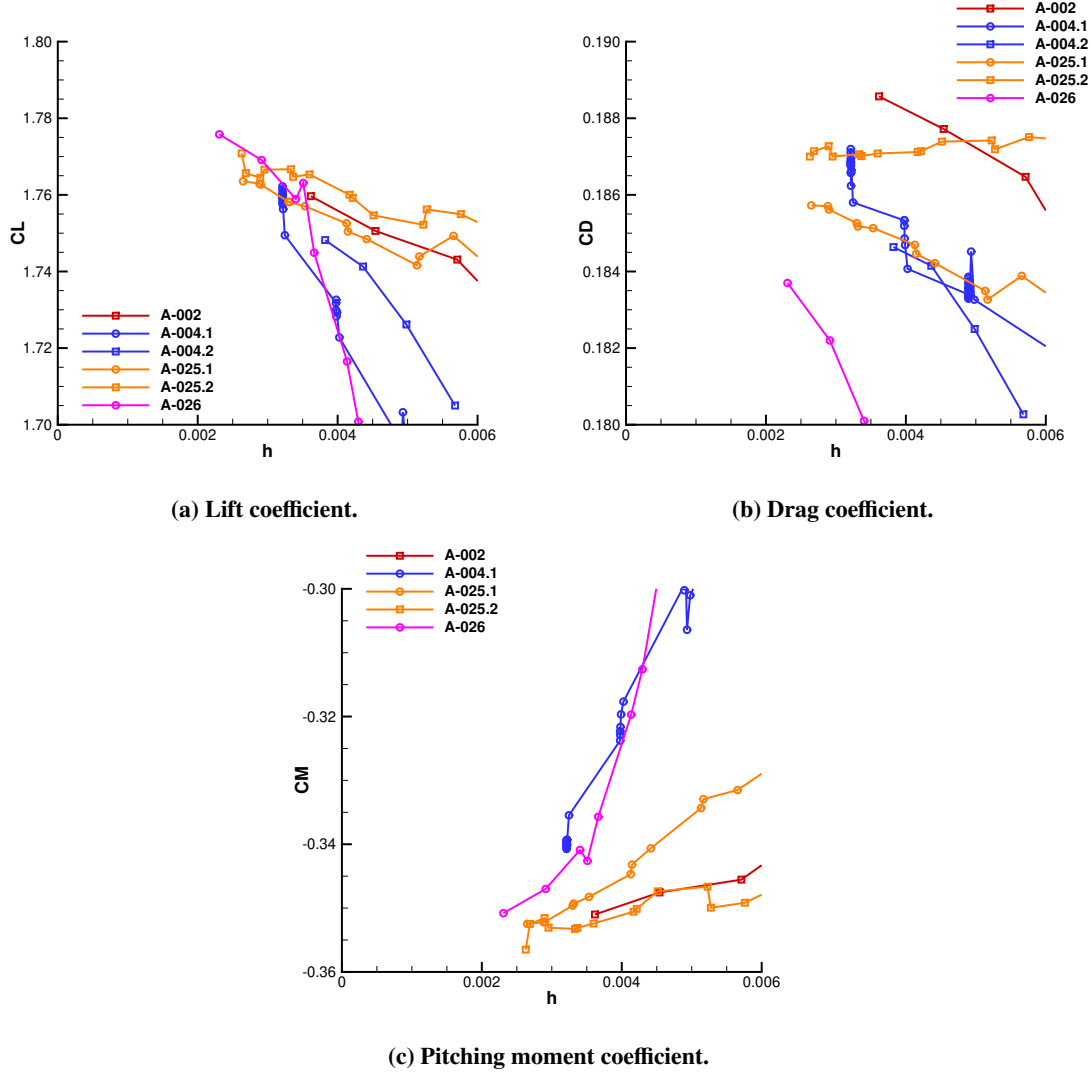


**Fig. 3 Mesh convergence of the CRM-HL at 7.05° angle of attack.**

CFD view 1 of total skin friction contours is shown for four submissions in Fig. 4. The submission identifier from Table 1, the mesh size, and the metric formulation are provided in each subfigure caption. The slat bracket wakes create stripes on the upper surface of the wing. The wakes of the flap track fairings interfere with the flow through the gap between the main element and flaps. These wakes create a wedge shaped separated flow region of low skin friction or black contour on the flap. The steps in the leading edge of the main element where the inboard and outboard ends of both flap segments integrate into the cruise shape create vortices that scrape the upper surface boundary layer. The nacelle chine corner vortices imprint on the nacelle. These features are consistent between submissions and the slat bracket wakes are the less distinct for A-025.1 and A-026.

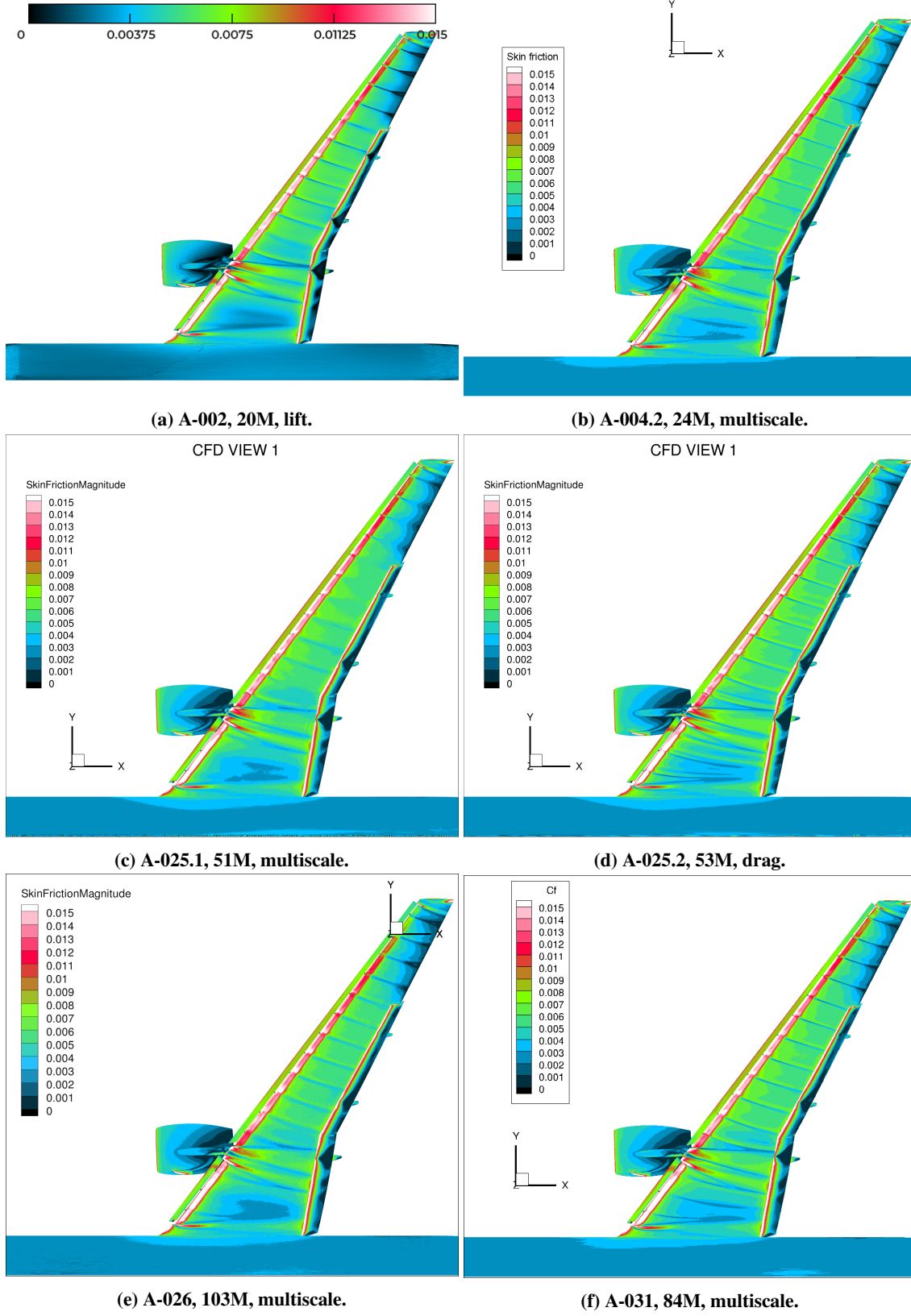


**Fig. 4** CFD view 1 of CRM-HL skin friction magnitude contours at  $7.05^\circ$  angle of attack.

The pressure coefficient for the finest mesh in the Fig. 3 mesh convergence trajectories is shown in Fig. 5. The extraction locations are shown in Fig. 5i. Excellent agreement is shown by the five submissions that provided pressure coefficient submissions, and a few localized differences are identified. The center of the inboard wing (span location B) is shown in the first row of Fig. 5. The inboard flap shows a less negative pressure coefficient peak for A-026 and a flat aft pressure (indicating flow separation) for A-031 in Fig. 5c. The center of wing (span location E) is shown in the middle row of Fig. 5. A-026 has a slightly different values for the lower surface and cove of slat in Fig. 5d. The outboard flap shows a less negative pressure coefficient peak for A-026 and a decreasing aft pressure (indicating less flow separation) for A-026 and A-031 in Fig. 5f. The outboard wing (span location G) is shown in the last row of Fig. 5. A-002 and A-026 have a slightly different values for the lower surface and cove of slat in Fig. 5d. The tailing edge of the main element upper surface has 0.2 pressure coefficient variation in Fig. 5e.

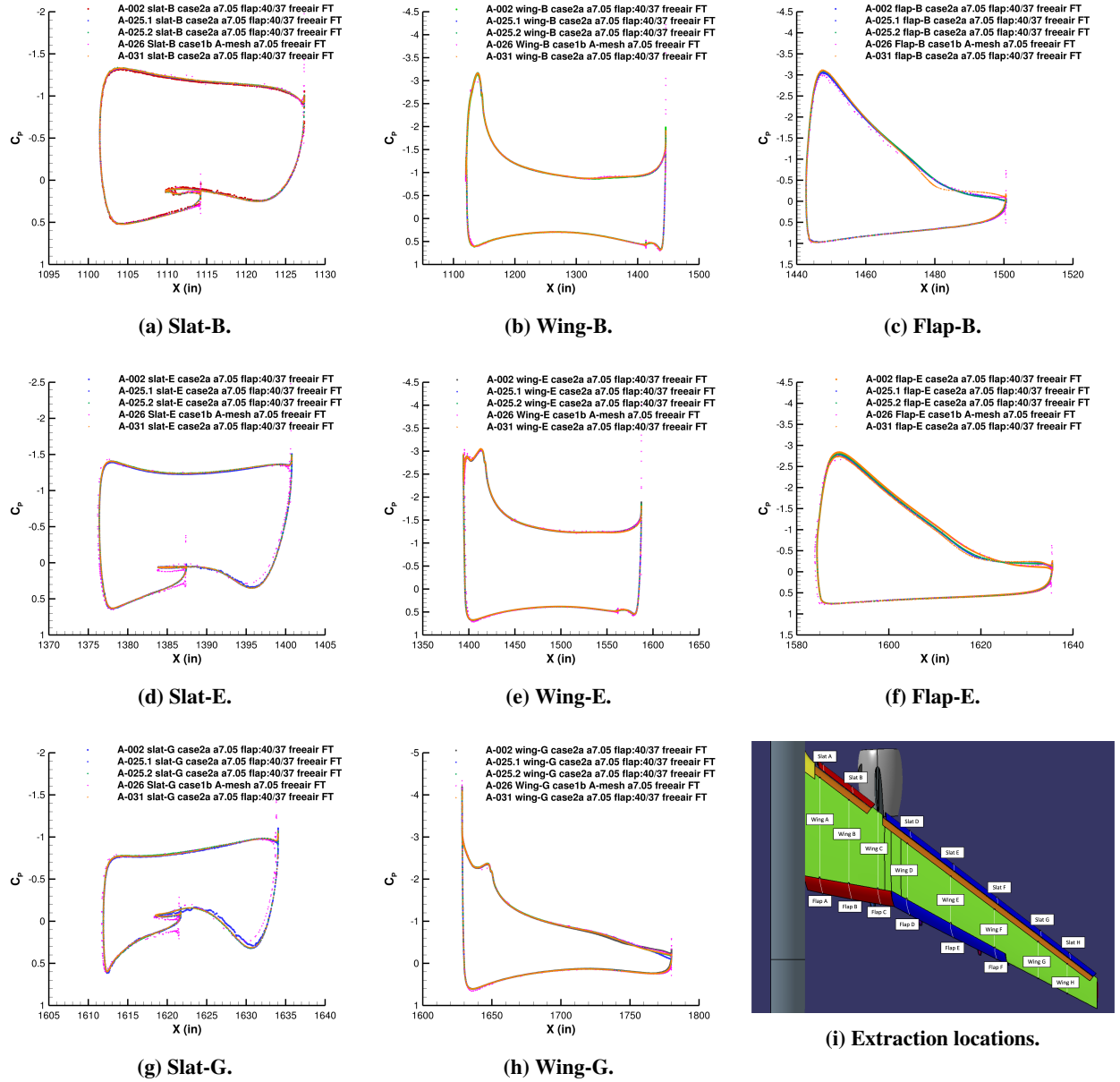


**Fig. 5** Fine mesh CRM-HL pressure coefficient at 7.05° angle of attack.

## V. Angle of Attack Range

The angle of attack range is shown in Fig. 6 for the ADAPT submissions marked best practice. See Section VIII for these ADAPT submissions in the context of the other TFG results. To declutter the plot, every tenth symbol ( $1^\circ$  spacing) is shown for the A-004.1 submission. The A-004.1 noted incomplete iterative convergence, particularly for the SA equation. Incomplete iterative convergence may be preventing the abrupt loss of lift and more negative pitching moment shown post-stall by the other submissions with more complete iterative convergence. The drag polar shown in Fig. 6b collapses the scatter at  $2.78^\circ$  and reduces the difference with the experiment at  $11.29^\circ$  for some participants. A-004.1 shows a higher lift/drag in Fig. 6b and more negative pitching moment in Fig. 6c approaching maximum lift coefficient than submissions with machine-level iterative convergence. The majority of the submissions used complexity continuation where each angle of attack is an independent case with free stream initial conditions. A-004.1 used angle of attack continuation at fixed complexity. A-004.2 used of complexity continuation for low angles of attack and a combination of angle of attack continuation and complexity continuation for high angles of attack. The ADAPT TFG submissions predicted a lower lift than experiment at high angles of attack before and at maximum lift, which may be a result of differences in flow separation patterns discussed in Section VII.

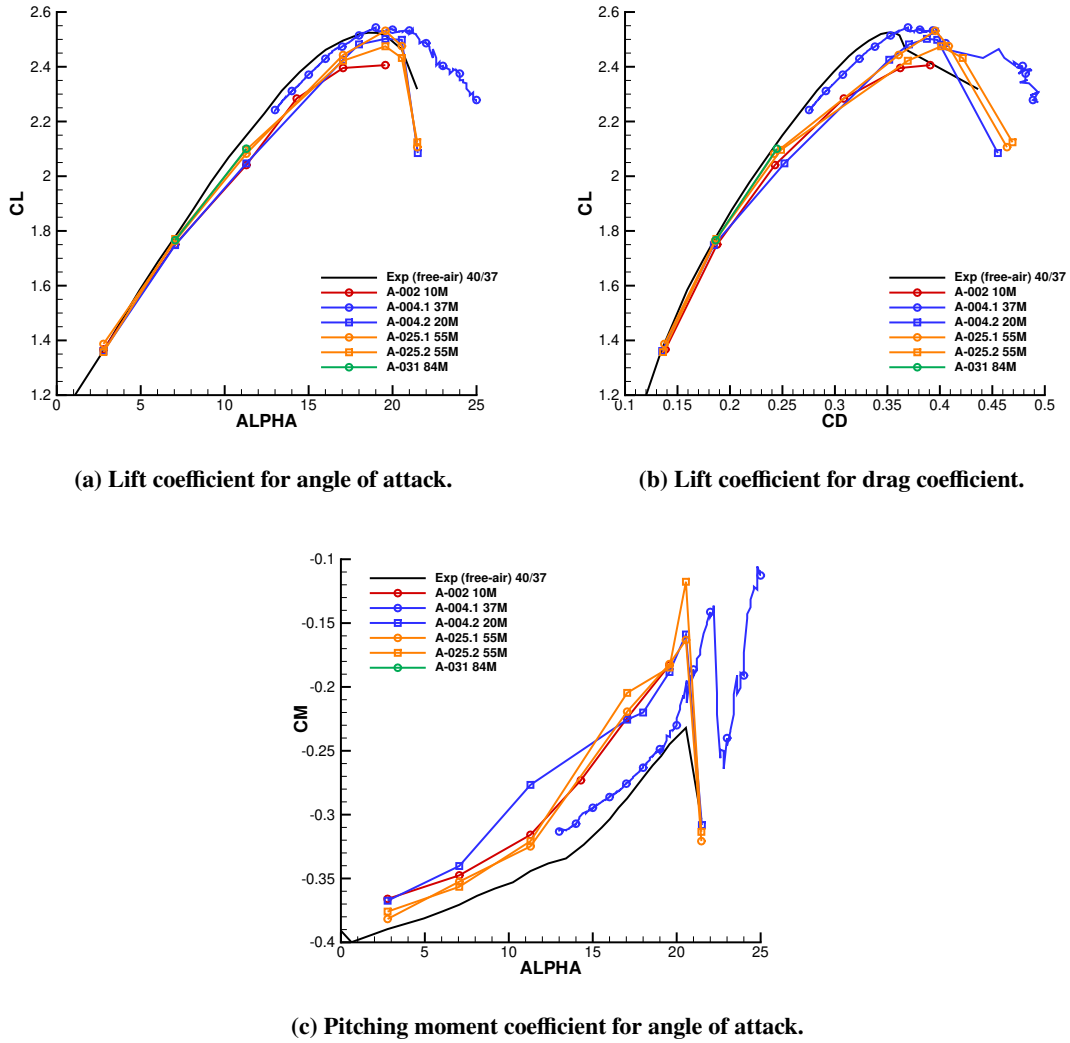
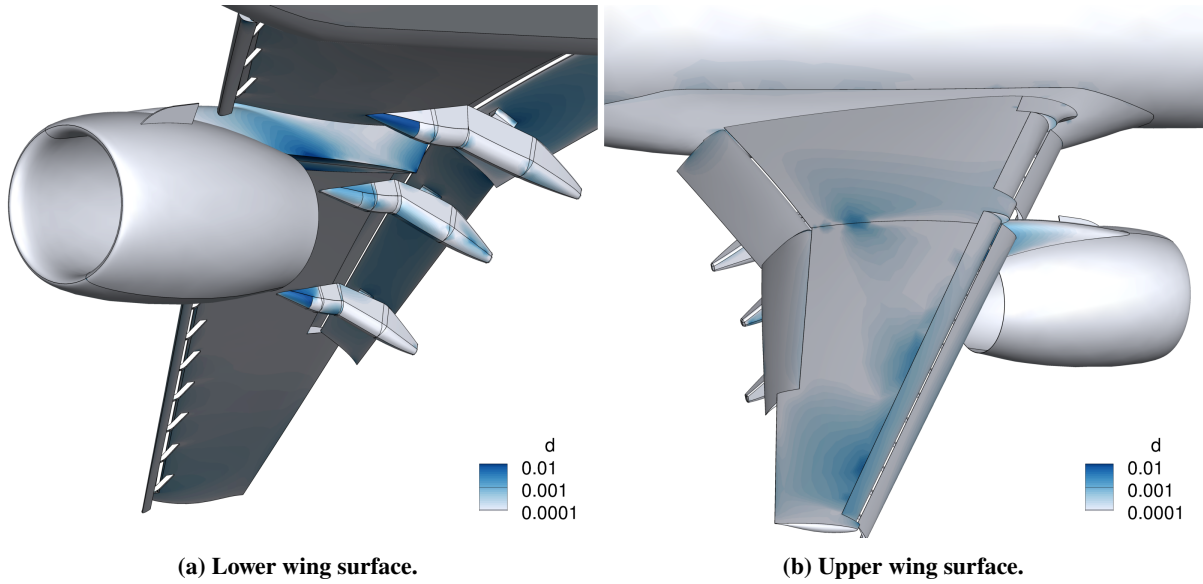


Fig. 6 CRM-HL angle of attack range, best-practice ADAPT TFG.

## VI. Best Practices

The MCAD model for the CRM-HL required significant interpretation to create the solid model provided to participants [56]. A boundary representation of a solid is constructed of curve geometry underlying edge topology and trim curves projected to surfaces to define the model faces [82]. Boundary representation tolerances are the distance between the edge curves and the trim curves evaluated on the surfaces. A majority of the boundary representation tolerances shown in Fig. 7 are larger than workshop meshing guidelines and adaptive meshing requirements [55]. Wing under slat surface (WUSS), pylon, and flap track fairings have the loosest tolerances. Many expert-guided mesh generation approaches accommodate these regions of loose tolerance by limiting the minimum tangential spacing in an effort to step over the ambiguity. Adaptive mesh techniques often interpret loose tolerances as contributions to the error estimation procedure and fail when geometry ambiguities are resolved. Geometry surrogates provide a continuous interpretation of the geometry in the neighborhood of these boundary representation tolerance hot spots and are designed to be accurate (or use the original geometry source) where boundary representation tolerances are tighter than mesh size requests.



**Fig. 7 CRM-HL geometry model boundary representation tolerance (in.).**

Small increments in angle of attack (angle of attack continuation) [35] appeared to aid nonlinear solvers that were unable to reach machine-level iterative convergence, diverged, or produced solutions with massive separation. Participants with stronger nonlinear solvers reported the ability to start the adaptive mesh sequence (complexity continuation) from free stream initial conditions.

The forces and moments for goal-oriented methods on coarse meshes converge faster to fine-mesh solutions than multiscale methods. Multiscale methods required more subiterations at a fixed complexity than goal-oriented methods. Goal-oriented methods are able to propagate slat wakes with less mesh and fewer subiterations than multiscale methods. Experiments with multiscale methods that use a partially converged goal-oriented mesh as the initial mesh show the benefit of early goal-oriented subiterations on later multiscale meshes. Barriers to the application of goal-oriented methods included not having an adjoint solver for a flow code, having discrete adjoint that is dual inconsistent, and difficulty converging the primal and dual flow equations.

## VII. Multiple Solutions

The locations of suspected multiple solutions are shown in Fig. 8. The sensitivity of each location changes with angle of attack. These locations are identified in early calculations shared in ADAPT meetings. Some of these locations have resolved into a common solution obtained by a majority of ADAPT participants with adaptive mesh refinement. The uniqueness of other locations is unclear in the ADAPT submissions. The trend of resolving these observed multiple solutions into common solutions with mesh refinement is encouraging. In cases where SA solutions are different from

experiment and consistent with each other, there may exist an opportunity to explore existing modifications to SA or propose new modifications to improve prediction of experimental measurements. If a sufficient level of consistency can be obtained for other RANS turbulence models, direct examination of modeling assumptions can be observed free from the influence of mesh effects. Many of the existing turbulence models were developed in the presence of uncontrolled and possibly large discretization or iterative errors.

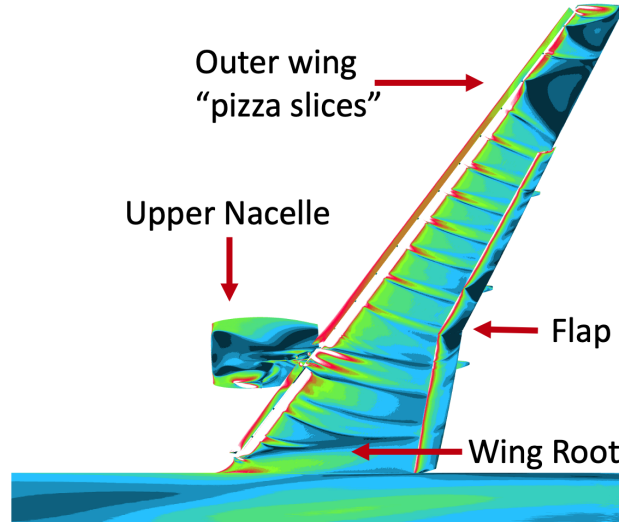


**Fig. 8** Suspected multiple solution locations.

### A. Flap Separation

The  $7.05^\circ$  angle of attack test case is challenging, because the flap is highly loaded. Two regions of concern were identified with initial calculations shared within ADAPT. The locations where the inboard flap meets the fuselage and where the inboard flap meets the outboard flap showed evidence for multiple separation patterns at  $7.05^\circ$  angle of attack. The experimental oil flow (at the uncorrected,  $5.98^\circ$  in-tunnel angle of attack) shows attached flow to the midchord of the flap for the majority of the inboard and outboard flap span, see Fig. 9. The upper flap boundary layer where the inboard flap meets the fuselage appears to be attached over the entire chord.

With additional mesh refinement, the majority of submissions show a small separated pocket (black contour) where the inboard flap end meets the fuselage in Fig. 10. The majority of the submissions show attached flow where the inboard flap meets the outboard flap.

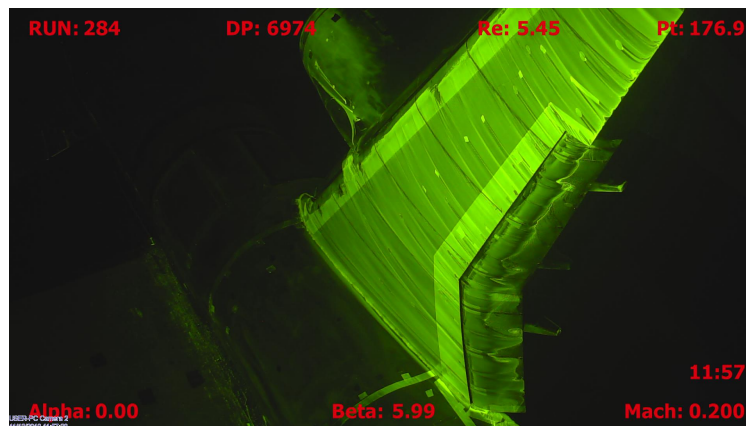


**Fig. 9** Oil flow,  $5.98^\circ$  in-tunnel angle of attack.



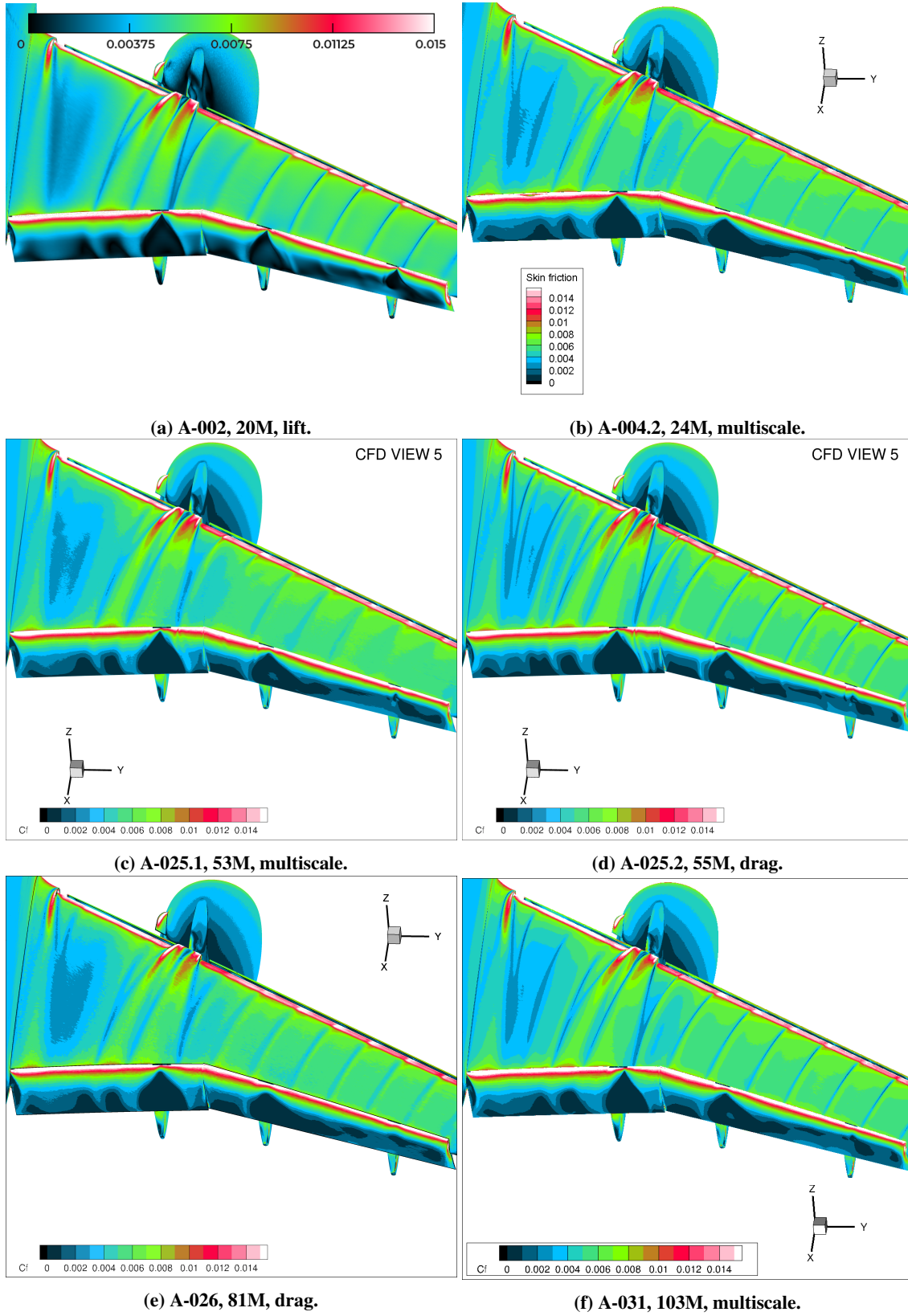


**Fig. 10** CFD view 5 of CRM-HL skin friction magnitude contours at  $7.05^\circ$  free air angle of attack.

## B. Outer Wing Separation

The upper wing surface outboard of the flaps of the CRM-HL has large triangular separation regions with SA and other RANS turbulence models for larger angles of attack, see examples in Fig. 11. These separation regions have been nicknamed “pizza slices” by the simulation community. The pizza slices are initiated by the slat bracket wakes near the leading edge of the main element. Smaller separation regions are seen in the wind tunnel oil flow patterns, Fig. 11d. The wind tunnel separation regions also align with the slat bracket wakes and initiate after 50% chord. In simulations, these pizza slices appear as low as  $10.5^\circ$  angle of attack and grow in area with increasing angle of attack. Their extent is influenced by incomplete iterative convergence and insufficient mesh resolution.

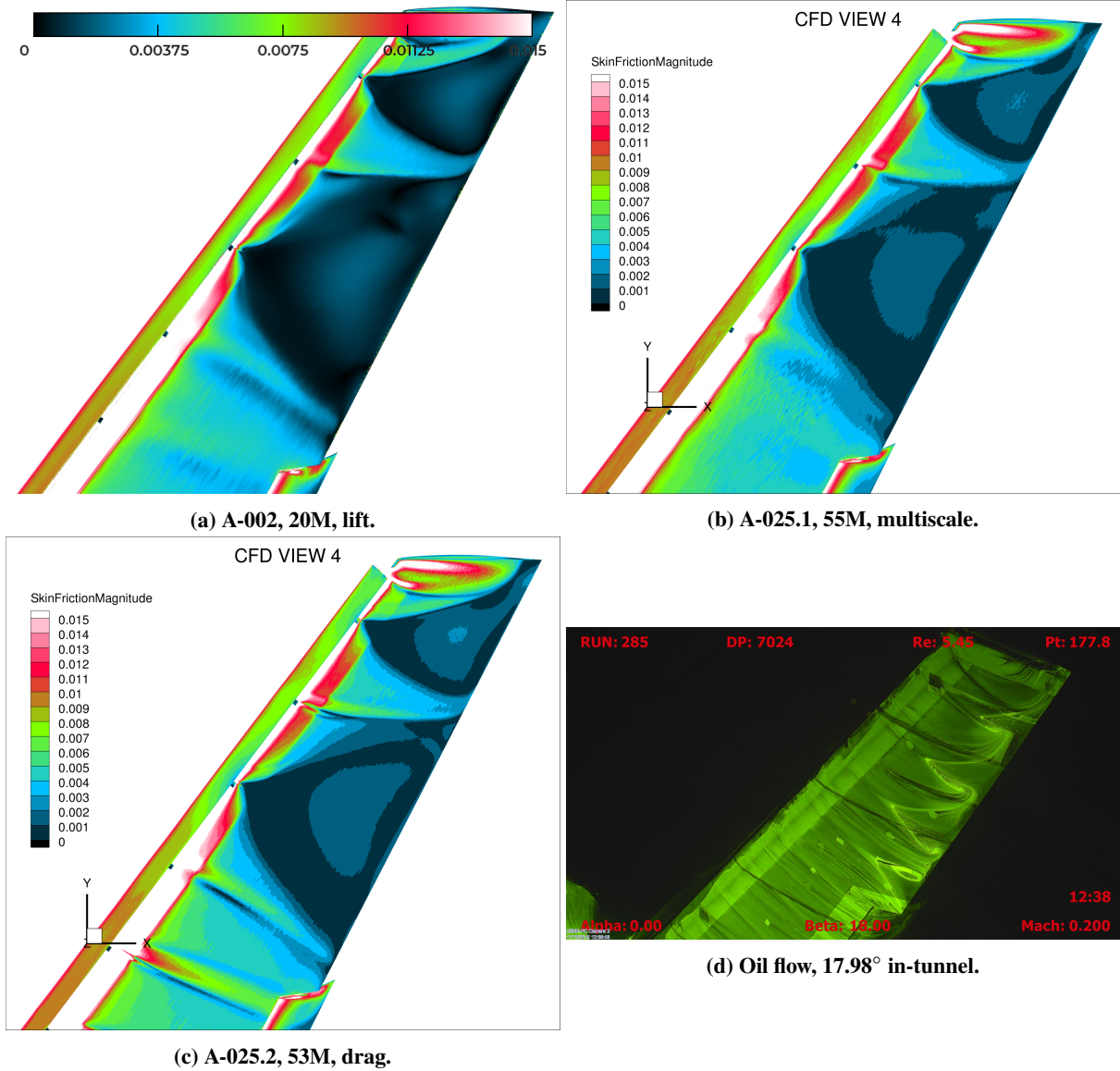


**Fig. 11** CFD view 4 of CRM-HL skin friction magnitude contours at  $19.57^\circ$  angle of attack.

The upper surface of the outer wing is shown for  $19.57^\circ$  angle of attack in Fig. 11. While the submissions do not match the wind tunnel oil flow in Fig. 11d, the ADAPT submissions are remarkably similar. Two independent flow solvers, two independent remeshers, and three independent metrics produced the same topology. This common solution is obtained with sufficient mesh resolution. Multiple solutions are observed at coarser mesh resolutions or with incomplete iterative convergence.

At  $20.55^\circ$  angle of attack, the separation pattern topology is unique for each submission, see Fig. 12. The A-025.1

submission shows the same pattern at  $19.57^\circ$  and  $20.55^\circ$  angles of attack. The separation patterns in the oil flow have increased in size between  $17.98^\circ$  and  $19.97^\circ$  angles of attack, but they are significantly smaller than the CFD results.

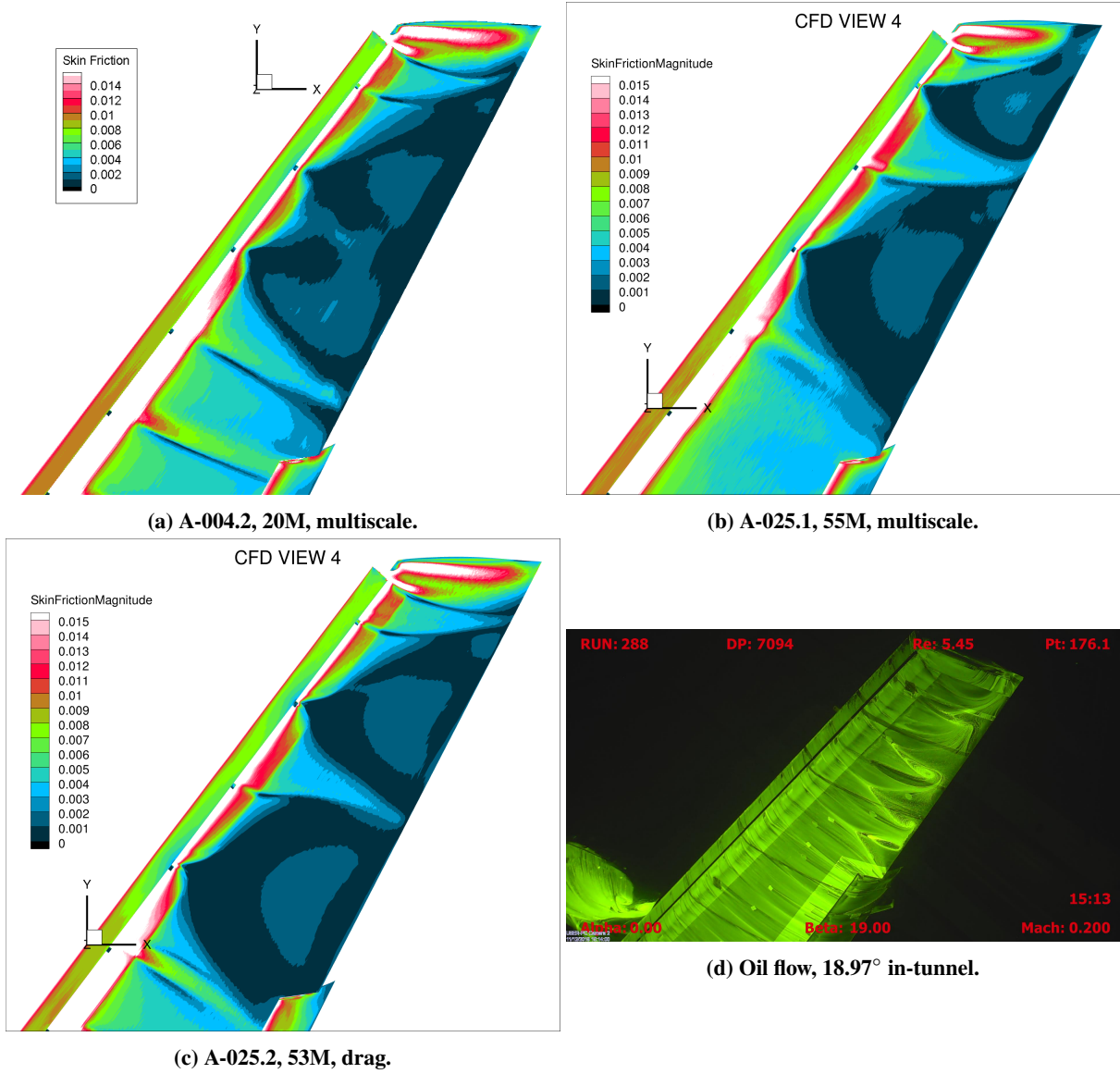
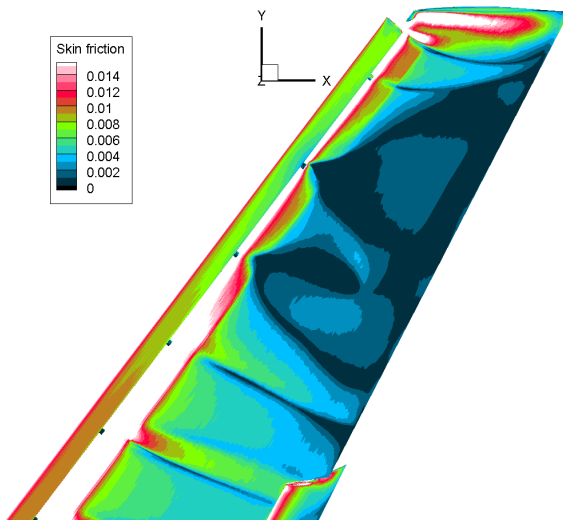
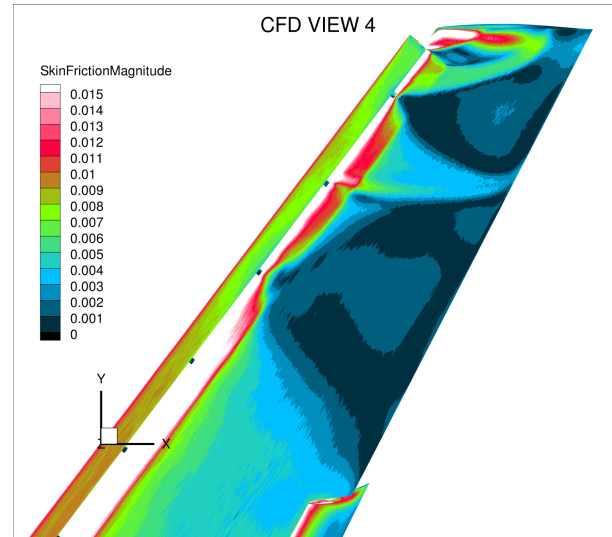


**Fig. 12** CFD view 4 of CRM-HL skin friction magnitude contours at  $20.55^\circ$  angle of attack.

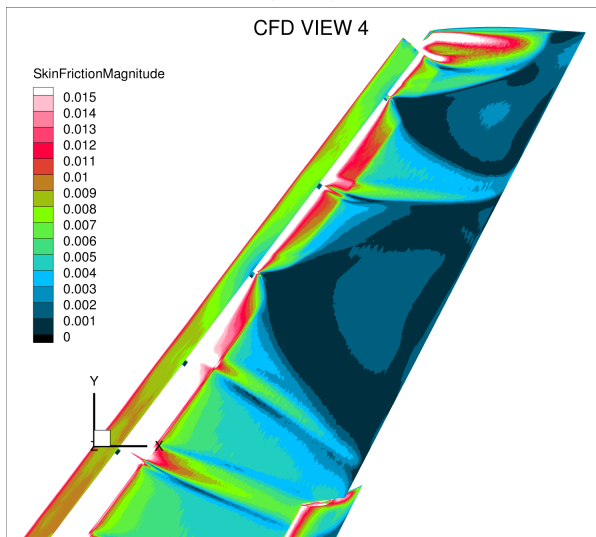
At  $21.47^\circ$  angle of attack, Fig. 13, the separation pattern topology is the same for A-025.1 and A-025.2. The A-025 submissions initiated mesh adaptation with free stream initial conditions. The A-004.2 submission shows the same pattern at  $20.55^\circ$  and  $21.47^\circ$  angle of attack. The separation patterns in the oil flow have increased in size between  $18.97^\circ$  and  $19.98^\circ$  angle of attack, but again they are significantly smaller than the submissions.



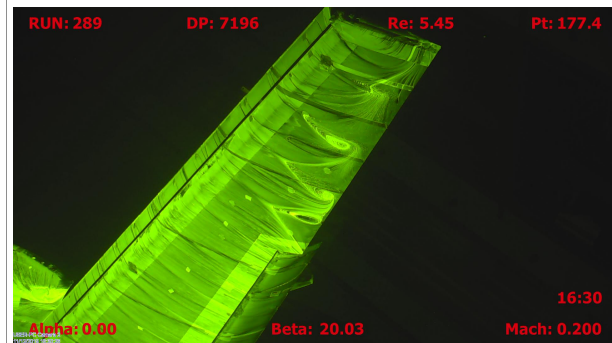
(a) A-004.2, 17M, multiscale.



(b) A-025.1, 55M, multiscale.



(c) A-025.2, 53M, drag.



(d) Oil flow, 19.98° in-tunnel.

**Fig. 13** CFD view 4 of CRM-HL skin friction magnitude contours at 21.47° angle of attack.



### C. Upper Nacelle and Wing Root Separation

At  $11.29^\circ$  angle of attack, the nacelle appears attached for three participants, see Fig. 14. There is a small separation region starting at the nacelle leading edge and a different separation pattern at the inboard tip of the flap where it meets the fuselage for submission A-002. The slat wakes are diffuse for submissions A-002 and A-025.1.

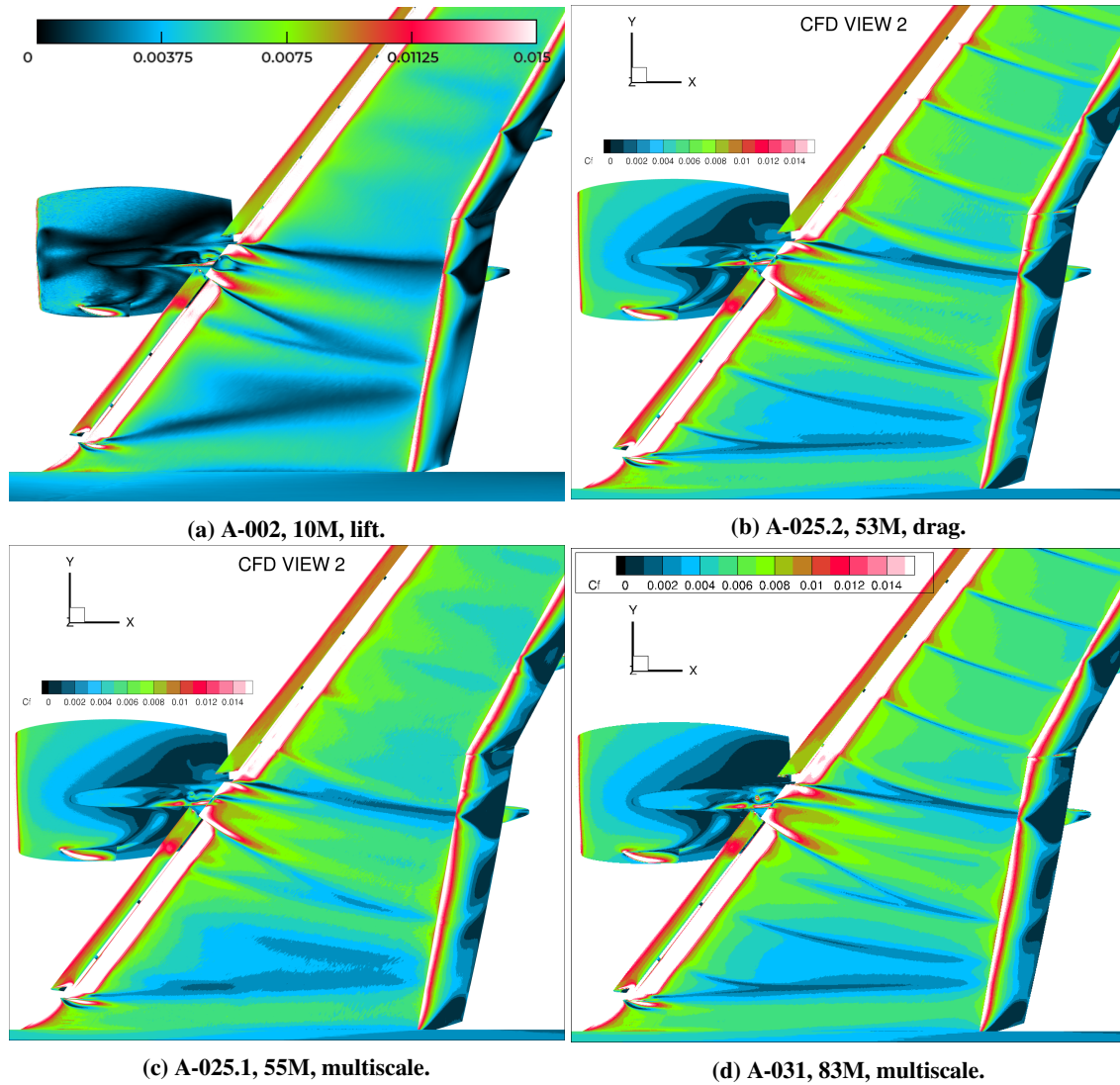


Fig. 14 CFD view 2 of CRM-HL skin friction magnitude contours at  $11.29^\circ$  angle of attack.

At  $19.57^\circ$  angle of attack, all the submissions show separation on the forward part of the nacelle, see Fig. 15. The separation region was delayed until the leading edge of the pylon for submission A-025.1. The wind tunnel oil flow image indicates attached flow until the corner flow between the nacelle and pylon for  $17.98^\circ$  in-tunnel angle of attack, see Fig. 15d.

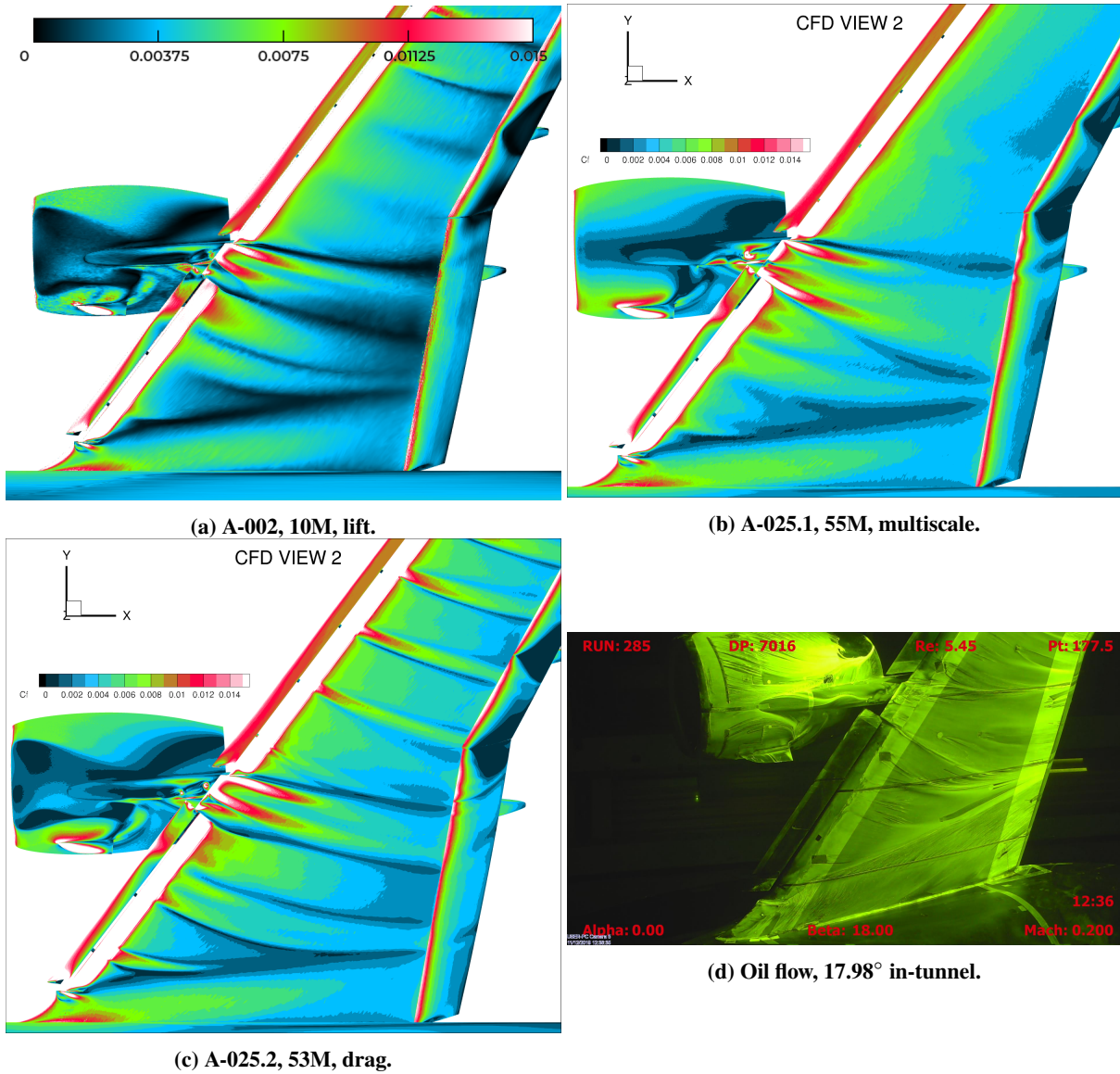
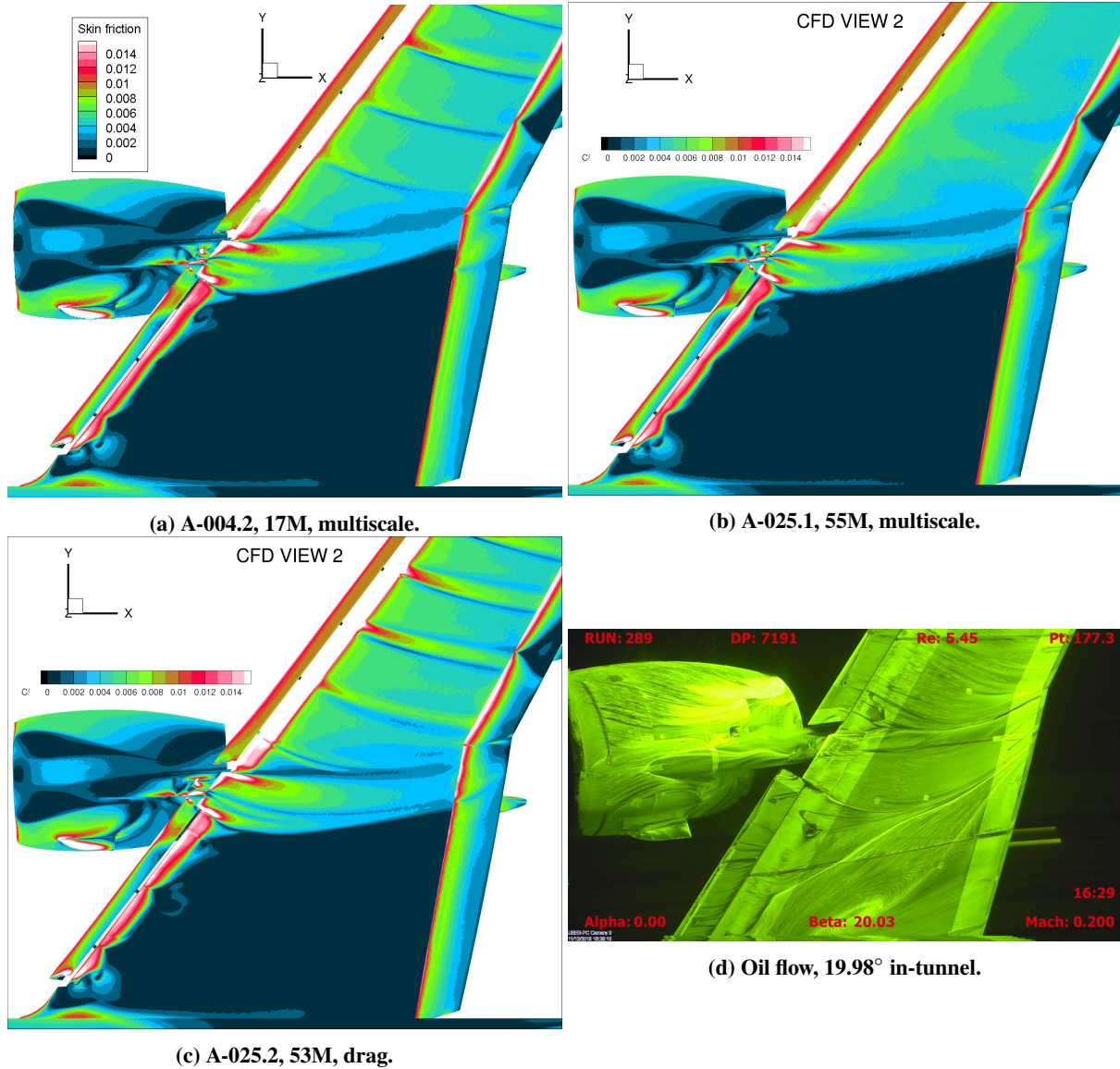


Fig. 15 CFD view 2 of CRM-HL skin friction magnitude contours at  $19.57^\circ$  angle of attack.

At  $21.47^\circ$  angle of attack, wing root separation is the expected stall mechanism based on wind tunnel oil flow images, see Fig. 16d. The abrupt formation of the wing root separation creates more negative pitching moment, see Fig. 6c. The separation topology (black skin friction contour) is consistent for the three submissions. There are differences between this common simulated skin friction contour topology and the wind tunnel oil flow images at  $19.98^\circ$  in-tunnel angle of attack, see Fig. 16d. The CFD community has come to the consensus that linear (Boussinesq) turbulence models, such as SA, will generally produce unrealistic juncture separation results when using finer meshes along with accurate numerics [83]. The wind tunnel oil flow indicates attached flow on the upper surface of the nacelle and a small wing root separation region. The wind tunnel test was performed with a half-span model attached to the wind tunnel wall and a peniche filled the space between the half-span model and the wall [20]. The interaction of the wind tunnel wall boundary layer and the half-span model may create differences to free-air CFD calculations.



**Fig. 16** CFD view 2 of CRM-HL skin friction magnitude contours at  $21.47^\circ$  angle of attack.

## VIII. Contributions

Solution adaptive methods provide a good source of reference solutions for use in CFD development and verification. Multiple independent implementations of flow solver, metric, and mesh mechanics converge to a common solution. The multielement airfoil verification case forces converge faster to fine-mesh values with mesh adaptation than uniformly refined expert-crafted meshes, see Section III.

The ADAPT submissions for 3D CRM-HL mesh convergence study at  $7.05^\circ$  angle of attack are combined with the SA “best practice” submissions for HRLES and RANS TFGs in Fig. 17. All the “best practice” WMLES/LBM are also included. The vertical axis scales were expanded in Fig. 17 as compared to the ADAPT submissions in Fig. 3. The variation between the ADAPT submissions is smaller than the other TFGs. The average mesh size is also smaller for ADAPT than other TFGs in terms of number of vertices.

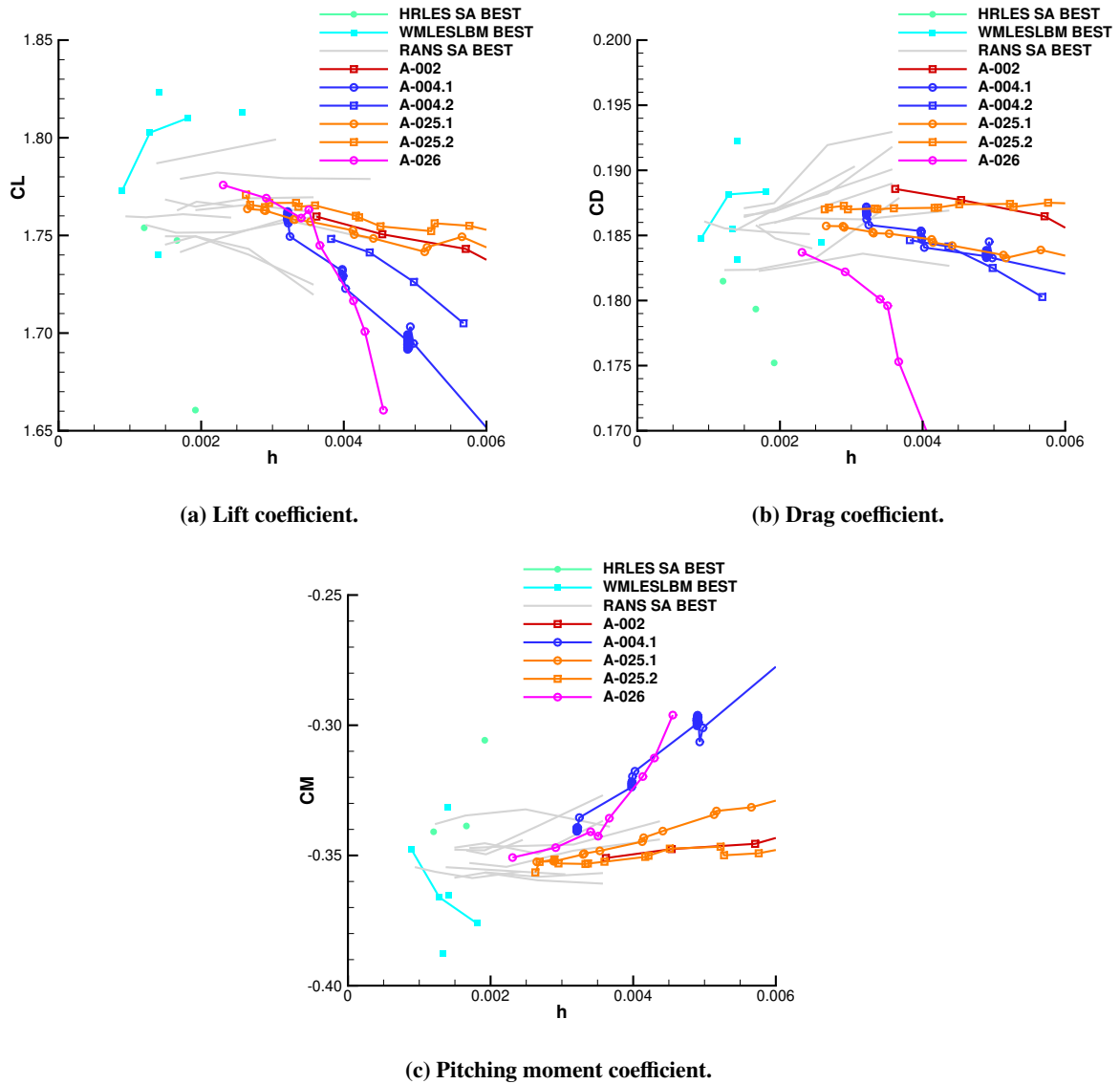
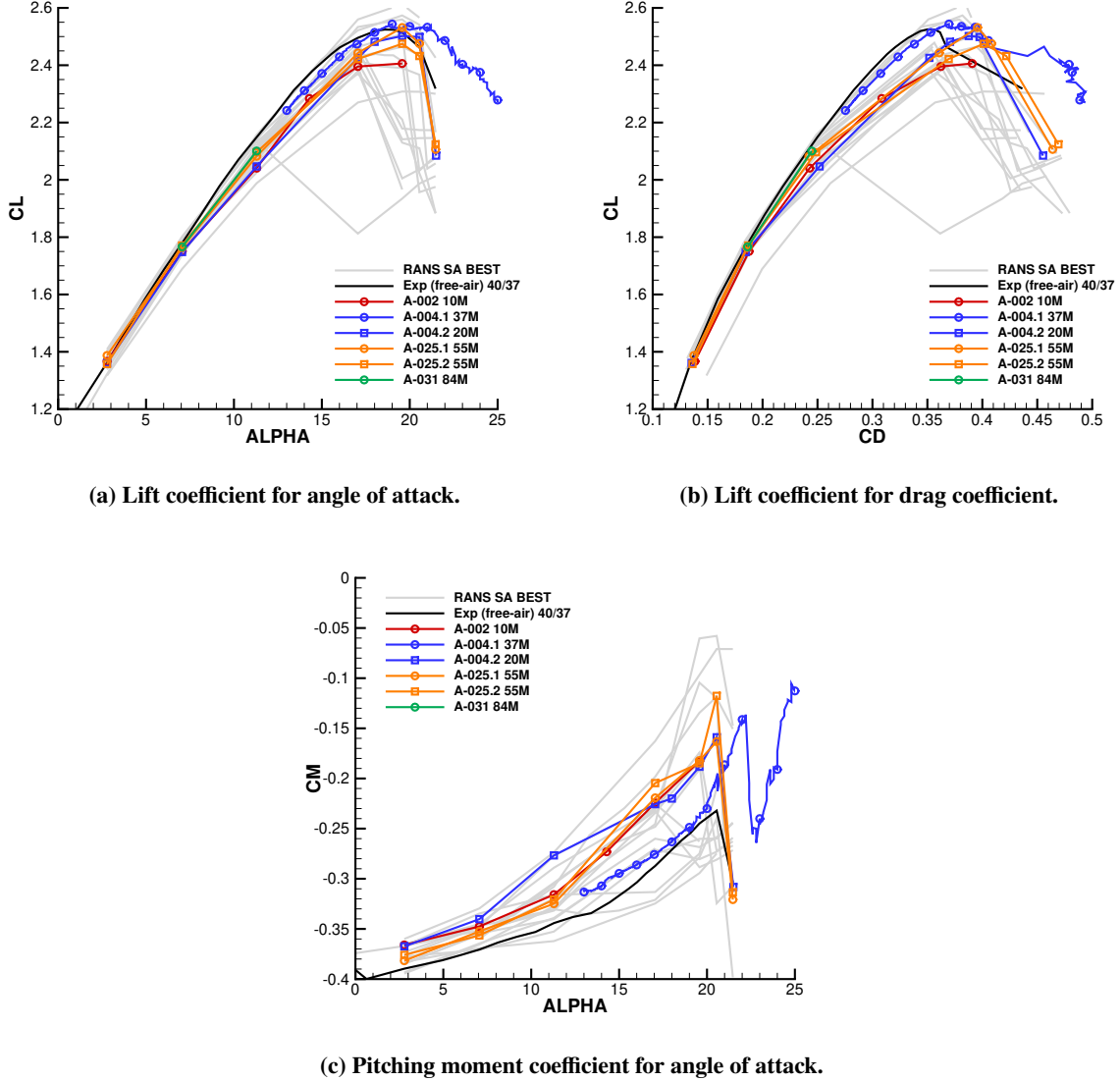


Fig. 17 Mesh convergence of CRM-HL at  $7.05^\circ$  angle of attack with other TFG results.

ADAPT TFG force and moment submissions are compared to RANS submissions in Fig. 18 for a range of angles of attack. SA “best practice” force and moment polar submissions for RANS are included as gray lines in Fig. 18. The ADAPT submissions are shown with the free-air corrected experimental measurements in Fig. 6. The ADAPT submissions have lower variation, particularly near maximum lift.

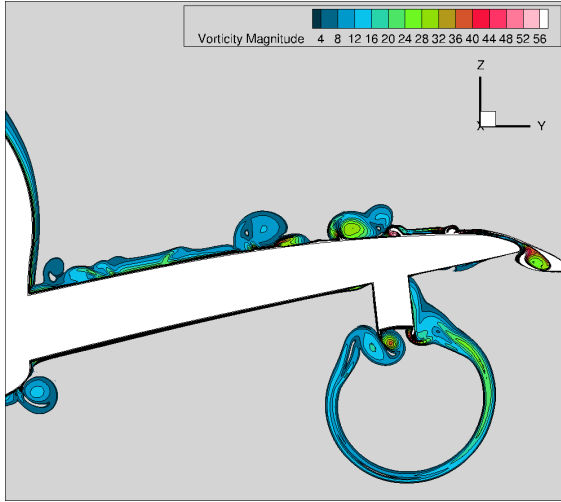


Multiple solutions for RANS are discussed in Section VII. While the separation topology inferred from the skin friction contours are different than the separation topology inferred from experimental oil flows, some degree of consistency amongst the ADAPT submissions was observed. This confirms that RANS with SA has limited prediction accuracy for this configuration at higher angles of attack. The consistency of results suggests that there may be more precision available with solution adaptive methods than the methods employed by other TFGs. Evaluating turbulence models with controlled discretization error (and iterative error) may lead to a better understanding of the application of these models. Further understanding may lead to modifications and enhancements to current models or new model development.

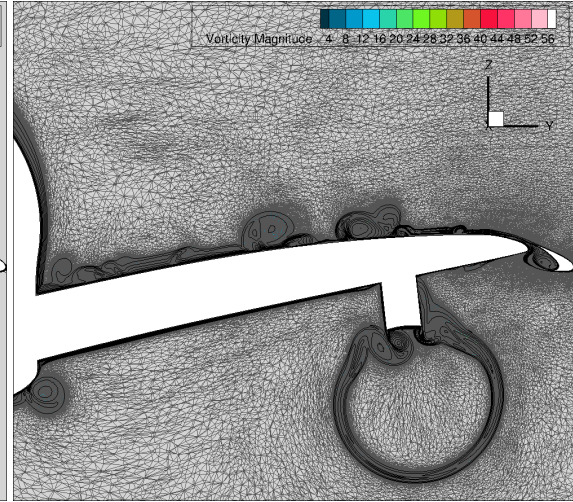


**Fig. 18 CRM-HL angle of attack range with other TFG results.**

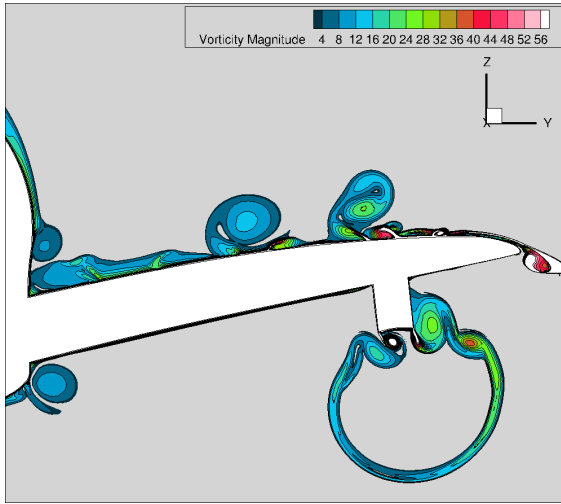
The  $x = 1275$  in. fuselage station is intersected with the vorticity magnitude and volume mesh to create CFD view 13 in Fig. 19. Unstructured mesh adaptation resolves the vortices and shear layers indicated by total vorticity contours. This imprints of these complex three dimensional flow structures are seen in the skin friction contours, for example see Figs. 10 and 14. The nacelle wake, nacelle chine, wing root, slat, and slat ends produce shear layers and vortices. These structures that evolve with angle for attack would be difficult to resolve with manual mesh resolution specification.



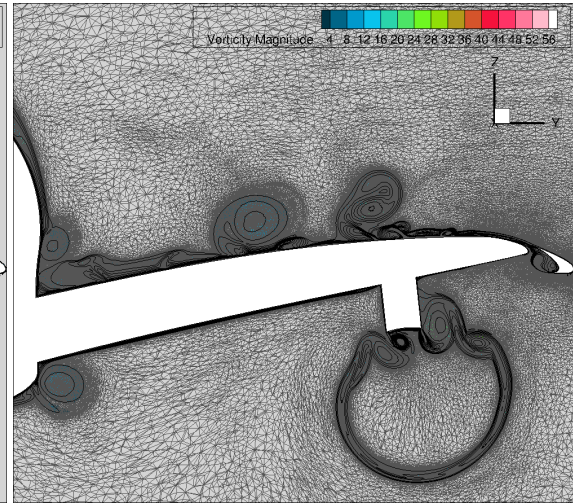
(a) A-031, 83M, multiscale, 7.05° angle of attack.



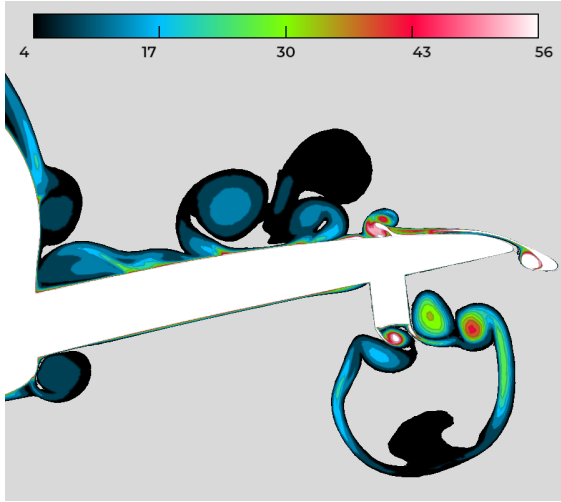
(b) A-031, 83M, multiscale, 7.05° angle of attack, mesh.



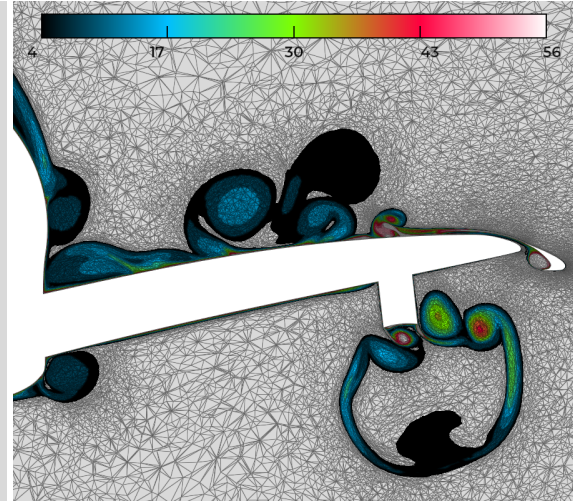
(c) A-031, 83M, multiscale, 11.29° angle of attack.



(d) A-031, 83M, multiscale, 11.29° angle of attack, mesh.



(e) A-002, 10M, lift, 17.05° angle of attack.



(f) A-002, 10M, lift, 17.05° angle of attack, mesh

Fig. 19 CFD view 13 of CRM-HL vorticity magnitude contours and mesh slices.

## IX. Summary

Evidence is provided to address the key questions of the ADAPT TFG. The sections are organized to provide ready access to this evidence.

**Can adaptive mesh convergence be achieved on the CRM-HL model across the angle of attack range?** The airfoil verification test case presented in Section III shows convincing mesh convergence for a 2D multielement airfoil at  $16^\circ$  angle of attack. ADAPT dedicated a significant effort to the CRM-HL at  $7.05^\circ$  angle of attack, see Section IV. While mesh convergence is unconvincing at the presented mesh sizes, variation between ADAPT submissions was lower than the submissions of other TFGs in Fig. 17. Initial concerns of multiple solutions manifested as differences in boundary layer separation topology appear to converge to a common topology on the flap with the application of solution-based mesh refinement, see Section VII.A. Excellent agreement is shown in pressure coefficient for the fine meshes of the mesh adaptation sequence at  $7.05^\circ$  angle of attack in Fig. 5, and a few minor differences were localized to slat and flap trailing edges.

The entire angle of attack range of the CRM-HL was a secondary objective of the ADAPT TFG. Section V shows the angle of attack range submissions and Fig. 18 places the ADAPT TFG submissions in the context of RANS TFG submissions. The variation between ADAPT submission increased with angle of attack, and remained lower than the variation between RANS submissions. The resolution of multiple boundary layer separation topologies to a single topology was partially achieved for the outer wing (Section VII.B) and nacelle (Section VII.C). A common topology was seen in some instances and a small number of topologies was seen for some flow conditions.

**What are the best practices, lessons learned, and outstanding technical issues for adaptive mesh modeling of high-lift applications (e.g., error estimate choice, flow solver settings, complexity schedule, solution continuation, geometry handling)?** Section VI details the learning and collaboration that the TFG model fostered. Some details are shared with all TFGs and some details are specific to unstructured mesh adaptation. The common themes are iterative convergence and documenting/accommodating loose boundary representation tolerances in the CRM-HL. The issues specific to ADAPT are details of the anisotropic metric formulation (e.g., goal-oriented or multiscale) and how complexity is scheduled with subiterations in a mesh refinement sequence.

**Can the causes of multiple solutions and techniques to encourage the “desired” branch be identified (e.g., incomplete iterative convergence, discretization error, initial conditions, solver settings)?** Section VII highlights the regions of the CRM-HL where multiple solutions or boundary layer separation topologies are suspected. These regions have an angle of attack range where the local solution has an increased sensitivity. Machine level iterative convergence appears to be a necessary ingredient to resolving a single topology. The flap appears to converge to a single topology, see Section VII.A. The outer wing (Section VII.B) and nacelle (Section VII.C) are less consistent with the current resolution of the ADAPT submissions. The wing root shows a massive separation in a similar mechanism as the wind tunnel oil flow, although the oil flow shows a smaller separation extent.

**Where can mesh adapted RANS contribute to prediction of high-lift flow physics?** This key question is intensionally open ended in comparison to the previous key questions. These contributions are listed in Section VIII. This section places the ADAPT submissions in the context of the submissions in other TFGs. The answers to the other key questions support the answer to this question. The potential for producing consistent solutions to high-lift flow fields is emerging. Early concerns about the differences between SA solutions and wind tunnel measurements distracted slightly from the goal of method verification in ADAPT. Once the “pizza slices” were accepted, the focus on verification could extend to the boundary layer separation topology as well as the total lift, drag, and pitching moment.

### A. Recommendations

There appears to be a degree of consistency in the solutions for SA from independent implementations in the ADAPT TFG, which is a significant improvement over previous HLPWs. The number of vertices and elements in the ADAPT TFG meshes are smaller than the meshes used by other TFGs. Improvements to the efficiency of flow solvers, metric calculations, and mesh adaptation may allow for larger mesh sizes and better mesh tailoring to resolve common solutions where multiple solutions are currently observed in ADAPT TFG solutions. Addressing the availability of high-performance computing resources will also accelerate learning. Many HLPW-4 participants cited difficulty in obtaining resources.

Mesh adaptation lowers the variation between CFD solutions as compared to expert-crafted meshes for steady RANS. This consistency sets the stage for verification of these methods for increasingly complex flows that include regions of boundary layer separation. Evaluation of different turbulence models and their corrections/variants may be possible with controlled discretization and iterative errors. The precision enabled by consistency created the potential to guide model development in an environment of minimal mesh effects. For example, the impact of subtle influences on expert-crafted mesh results like the turbulence model free stream boundary conditions can be isolated with mesh adaptation, which could result in explicit specification of turbulence model free stream boundary conditions in future workshops.

Scale-resolving WMLES and HRLES variation could also be lowered by mesh adaptation. Initial application of unstructured mesh adaptation to HRLES resulted in a reinforcement of the gray-area problem [49]. Continued research may lead to mesh automation with increases in reliability and consistency that synergistically reduces the negative aspects of the gray-area problem with meshing and HRLES algorithm improvements. The accommodation of wall models in error estimation for unstructured mesh adaptation may support WMLES and reduce the mesh sizes required for RANS. WMLES and the LES portions of WMLES appear to require low aspect ratio in the range of one to four [84]. Unstructured mesh adaptation methods have been optimized for extremely large aspect ratio to resolve the normal direction of boundary layers in RANS solutions. Scale-resolving simulation with lower aspect ratio requirements may increase the robustness and automation of geometry accommodation.

Formal verification of unit problems led to advancements before the workshop and the success of ADAPT. Simpler problems that allow simultaneous verification of RANS, ADAPT, HO, HRLES, and WMLES/SLB will foster collaboration between the TFGs. The tension between problems of sufficient complexity to be relevant to realistic flight vehicles and simple unit problems where incremental progress can be compounded is a perceived barrier. Overcoming this manufactured barrier will allow for accelerating the development of high-lift prediction methods and supporting the CbA revolution.

Maturing geometry surrogates [55] in the presence of loose boundary representation tolerances will have a direct impact on mesh adaptation robustness and reducing the cost of expert-crafted meshing. Improved nonlinear convergence in conjunction with methods with low dissipation ensure consistent results and obtaining a solution on a coarser mesh closer to a finer mesh solution. Improving the iterative convergence of dual-consistent discrete adjoint systems allows broader application of goal-oriented metrics. These goal-oriented methods show improved force convergence on coarse meshes over adjoint-free methods. Low dispersion and dissipation schemes are critical for the integration of unstructured mesh adaptation with WMLES and HRLES methods.

## Acknowledgments

The authors would like to thank the entire HLPW-4 organizing committee, TFG leaders, participants, observers, and attendees. The discussions during ADAPT TFG meetings and the workshop contribute to the content and recommendations of this summary. The authors appreciate the detailed feedback provided by Chris Rumsey (NASA), Aravind Balan (IIT Bombay), and Ryan Glasby (Oak Ridge National Lab). This work was partially supported by the Transformational Tools and Technologies (TTT) Project of the NASA Transformative Aeronautics Concepts Program (TACP) under the Aeronautics Research Mission Directorate.

## References

- [1] Smith, A. M. O., "High-Lift Aerodynamics," *AIAA Journal of Aircraft*, Vol. 12, No. 6, 1975, pp. 501–530. doi:10.2514/3.59830.
- [2] Rumsey, C. L., and Ying, S. X., "Prediction of High Lift: Review of Present CFD Capability," *Progress in Aerospace Sciences*, Vol. 38, No. 2, 2002, pp. 145–180. doi:10.1016/S0376-0421(02)00003-9.
- [3] Clark, A. M., Slotnick, J. P., Taylor, N., and Rumsey, C. L., "Requirements and Challenges for CFD Validation within the High-Lift Common Research Model Ecosystem," AIAA Paper 2020–2772, 2020. doi:10.2514/6.2020-2772.
- [4] Slotnick, J., Khodadoust, A., Alonso, J., Darmofal, D., Gropp, W., Lurie, E., and Mavriplis, D., "CFD Vision 2030 Study: A Path to Revolutionary Computational Aerosciences," NASA CR-2014-218178, Langley Research Center, Mar. 2014. doi:2060/20140003093.
- [5] Slotnick, J. P., and Mavriplis, D. J., "A Grand Challenge for the Advancement of Numerical Prediction of High Lift Aerodynamics," AIAA Paper 2021–955, 2021. doi:10.2514/6.2021-0955.

- [6] Mauery, T., Alonso, J., Cary, A., Lee, V., Malecki, R., Mavriplis, D., Medic, G., Schaefer, J., and Slotnick, J., “A Guide for Aircraft Certification by Analysis,” NASA CR-20210015404, May 2021. doi:2060/20210015404.
- [7] Rumsey, C. L., Slotnick, J. P., and Woeber, C. D., “HLPW-4/GMGW-3: Overview and Workshop Summary,” Reston, VA (submitted for publication).
- [8] Rumsey, C. L., Slotnick, J. P., Long, M., Stuever, R. A., and Wayman, T. R., “Summary of the First AIAA CFD High-Lift Prediction Workshop,” *AIAA Journal of Aircraft*, Vol. 48, No. 6, 2011, pp. 2068–2079. doi:10.2514/1.C031447.
- [9] Slotnick, J. P., Hannon, J. A., and Chaffin, M., “Overview of the 1st AIAA CFD High Lift Prediction Workshop,” AIAA Paper 2011–862, 2011. doi:10.2514/6.2011-862.
- [10] Johnson, P. L., Jones, K. M., and Madson, M. D., “Experimental Investigation of a Simplified 3D High Lift Configuration in Support of CFD Validation,” AIAA Paper 2000–4217, 2000. doi:10.2514/6.2000-4217.
- [11] Hannon, J. A., Washburn, A. E., Jenkins, L. N., and Watson, R. D., “Trapezoidal Wing Experimental Repeatability and Velocity Profiles in the 14- by 22-Foot Subsonic Tunnel,” AIAA Paper 2012–706, 2012. doi:10.2514/6.2012-706.
- [12] Rumsey, C. L., and Slotnick, J. P., “Overview and Summary of the Second AIAA High Lift Prediction Workshop,” *AIAA Journal of Aircraft*, Vol. 52, No. 4, 2015, pp. 1006–1025. doi:10.2514/1.C032864.
- [13] Rudnik, R., Huber, K., and Melber-Wilkending, S., “EUROLIFT Test Case Description for the 2nd High Lift Prediction Workshop,” AIAA Paper 2012–2924, 2012. doi:10.2514/6.2012-2924.
- [14] Rumsey, C. L., Slotnick, J. P., and Sclafani, A. J., “Overview and Summary of the Third AIAA High Lift Prediction Workshop,” *AIAA Journal of Aircraft*, Vol. 56, No. 2, 2019, pp. 621–644. doi:10.2514/1.C034940.
- [15] Lacy, D. S., and Sclafani, A. J., “Development of the High Lift Common Research Model (HL-CRM): A Representative High Lift Configuration for Transonic Transports,” AIAA Paper 2016–308, 2016. doi:10.2514/6.2016-0308.
- [16] Yokokawa, Y., Murayama, M., Uchida, H., Tanaka, K., Ito, T., and Yamamoto, K., “Aerodynamic Influence of a Half-Span Model Installation for High-Lift Configuration Experiment,” AIAA Paper 2010–684, 2010. doi:10.2514/6.2010-684.
- [17] Chawner, J. R., Michal, T., Slotnick, J. P., and Rumsey, C. L., “Summary of the 1st AIAA Geometry and Mesh Generation Workshop (GMGW-1) and Future Plans,” AIAA Paper 2018–128, 2018. doi:10.2514/6.2018-0128.
- [18] Woeber, C. D., Masters, J. S., and McDaniel, D. R., “Summary of Exascale and Remeshing Efforts for the Second Geometry and Mesh Generation Workshop,” AIAA Paper 2019–3458, 2019. doi:10.2514/6.2019-3458.
- [19] Lacy, D. S., and Clark, A. M., “Definition of Initial Landing and Takeoff Reference Configurations for the High Lift Common Research Model (CRM-HL),” AIAA Paper 2020–2771, 2020. doi:10.2514/6.2020-2771.
- [20] Evans, A., Lacy, D., Smith, I., and Rivers, M., “Test Summary of the NASA Semi-Span High-Lift Common Research Model at the QinetiQ 5-Metre Low-Speed Wind Tunnel,” AIAA Paper 2020–2770, 2020. doi:10.2514/6.2020-2770.
- [21] Spalart, P. R., and Allmaras, S. R., “A One-Equation Turbulence Model for Aerodynamic Flows,” *La Recherche Aéronautique*, Vol. 1, 1994, pp. 5–21.
- [22] Allmaras, S. R., Johnson, F. T., and Spalart, P. R., “Modifications and Clarifications for the Implementation of the Spalart-Allmaras Turbulence Model,” *Seventh International Conference on Computational Fluid Dynamics (ICCFD7)*, 2012.
- [23] Morrison, J. H., Kleb, B., and Vassberg, J. C., “Observations on CFD Verification and Validation from the AIAA Drag Prediction Workshops,” AIAA Paper 2014–202, 2014. doi:10.2514/6.2014-0202.
- [24] Levy, D. W., Laffin, K. R., Tinoco, E. N., Vassberg, J. C., Mani, M., Rider, B., Rumsey, C. L., Wahls, R. A., Morrison, J. H., Brodersen, O. P., Crippa, S., Mavriplis, D. J., and Murayama, M., “Summary of Data from the Fifth Computational Fluid Dynamics Drag Prediction Workshop,” *AIAA Journal of Aircraft*, Vol. 51, No. 4, 2014, pp. 1194–1213. doi:10.2514/1.C032389.
- [25] Park, M. A., Laffin, K. R., Chaffin, M. S., Powell, N., and Levy, D. W., “CFL3D, FUN3D, and NSU3D Contributions to the Fifth Drag Prediction Workshop,” *AIAA Journal of Aircraft*, Vol. 51, No. 4, 2014, pp. 2068–2079. doi:10.2514/1.C032613.
- [26] Yamamoto, K., Tanaka, K., and Murayama, M., “Effect of a Nonlinear Constitutive Relation for Turbulence Modeling on Predicting Flow Separation at Wing-Body Junction of Transonic Commercial Aircraft,” AIAA Paper 2012–2895, 2012.

- [27] Spalart, P. R., “Strategies for Turbulence Modelling and Simulations,” *International Journal of Heat and Fluid Flow*, Vol. 21, No. 3, 2000, pp. 252–263. doi:10.1016/S0142-727X(00)00007-2.
- [28] Murayama, M., Yamamoto, K., Hashimoto, A., Ishida, T., Uenoan, M., Tanaka, K., and Ito, Y., “Japan Aerospace Exploration Agency Studies for the Fifth AIAA Drag Prediction Workshop,” *AIAA Journal of Aircraft*, Vol. 51, No. 4, 2014, pp. 1244–1267. doi:10.2514/1.C032647.
- [29] Sclafani, A. J., Vassberg, J. C., Winkler, C. M., Dorgan, A. J., Mani, M., Olsen, M. E., and Coder, J. G., “Analysis of the Common Research Model Using Structured and Unstructured Meshes,” *AIAA Journal of Aircraft*, Vol. 51, No. 4, 2014, pp. 1223–1243. doi:10.2514/1.C032411.
- [30] Laffin, K. R., Klausmeyer, S. M., Zickuhr, T., Wahls, R. A., Morrison, J. H., Brodersen, O. P., Rakowitz, M. E., Tinoco, E. N., and Godard, J.-L., “Data Summary from Second AIAA Computational Fluid Dynamics Drag Prediction Workshop,” *AIAA Journal of Aircraft*, Vol. 42, No. 5, 2005, pp. 1165–1178. doi:10.2514/1.10771.
- [31] Vassberg, J. C., Tinoco, E. N., Mani, M., Brodersen, O. P., Eisfeld, B., Wahls, R. A., Morrison, J. H., Zickuhr, T., Laffin, K. R., and Mavriplis, D. J., “Abridged Summary of the Third AIAA Computational Fluid Dynamics Drag Prediction Workshop,” *AIAA Journal of Aircraft*, Vol. 45, No. 3, 2008, pp. 781–798. doi:10.2514/1.30572.
- [32] Kamenetskiy, D. S., Bussioletti, J. E., Hilmes, C. L., Venkatakrishnan, V., and Wigton, L. B., “Numerical Evidence of Multiple Solutions for the Reynolds-Averaged Navier-Stokes Equations,” *AIAA Journal*, Vol. 52, No. 8, 2014, pp. 1686–1698. doi:10.2514/1.J052676.
- [33] Loseille, A., and Alauzet, F., “Continuous Mesh Framework Part I: Well-Posed Continuous Interpolation Error,” *SIAM Journal on Numerical Analysis*, Vol. 49, No. 1, 2011, pp. 38–60. doi:10.1137/090754078.
- [34] Loseille, A., and Alauzet, F., “Continuous Mesh Framework Part II: Validations and Applications,” *SIAM Journal on Numerical Analysis*, Vol. 49, No. 1, 2011, pp. 61–86. doi:10.1137/10078654X.
- [35] Balan, A., Park, M. A., Wood, S. L., Anderson, W. K., and Jacobson, K. E., “Angle-of-Attack Sweep with Mesh Adaptation for High-Lift Configurations,” *AIAA Paper* 2022–218, 2022. doi:10.2514/6.2022-0218.
- [36] Loseille, A., Dervieux, A., Frey, P. J., and Alauzet, F., “Achievement of Global Second Order Mesh Convergence for Discontinuous Flows with Adapted Unstructured Meshes,” *AIAA Paper* 2007–4186, 2007. doi:10.2514/6.2007-4186.
- [37] Alauzet, F., and Loseille, A., “High-Order Sonic Boom Modeling Based on Adaptive Methods,” *Journal of Computational Physics*, Vol. 229, No. 3, 2010, pp. 561–593. doi:10.1016/j.jcp.2009.09.020.
- [38] Fidkowski, K. J., and Darmofal, D. L., “Review of Output-Based Error Estimation and Mesh Adaptation in Computational Fluid Dynamics,” *AIAA Journal*, Vol. 49, No. 4, 2011, pp. 673–694. doi:10.2514/1.J050073.
- [39] Balan, A., Park, M. A., Wood, S. L., Anderson, W. K., Rangarajan, A., Sanjay, D. P., and May, G., “A Review and Comparison of Error Estimators for Anisotropic Mesh Adaptation for Flow Simulations,” *Computers and Fluids*, Vol. 234, 2022, p. 105259. doi:10.1016/j.compfluid.2021.105259.
- [40] Alauzet, F., and Loseille, A., “A Decade of Progress on Anisotropic Mesh Adaptation for Computational Fluid Dynamics,” *Computer-Aided Design*, Vol. 72, 2016, pp. 13–39. doi:10.1016/j.cad.2015.09.005, 23rd International Meshing Roundtable Special Issue: Advances in Mesh Generation.
- [41] Park, M. A., Krakos, J. A., Michal, T., Loseille, A., and Alonso, J. J., “Unstructured Grid Adaptation: Status, Potential Impacts, and Recommended Investments Toward CFD Vision 2030,” *AIAA Paper* 2016–3323, 2016. doi:10.2514/6.2016-3323.
- [42] Galbraith, M. C., Caplan, P. C., Carson, H. A., Park, M. A., Balan, A., Anderson, W. K., Michal, T., Krakos, J. A., Kamenetskiy, D. S., Loseille, A., Alauzet, F., Frazza, L., and Barral, N., “Verification of Unstructured Grid Adaptation Components,” *AIAA Journal*, Vol. 58, No. 9, 2020, pp. 3947–3962. doi:10.2514/1.J058783.
- [43] Balan, A., Park, M. A., Anderson, W. K., Kamenetskiy, D. S., Krakos, J. A., Michal, T., and Alauzet, F., “Verification of Anisotropic Mesh Adaptation for RANS Simulations over ONERA M6 Wing,” *AIAA Journal*, Vol. 58, No. 4, 2020, pp. 1550–1565. doi:10.2514/1.J059158.
- [44] Michal, T., Krakos, J., Kamenetskiy, D., Galbraith, M., Ursachi, C.-I., Park, M. A., Anderson, W. K., Alauzet, F., and Loseille, A., “Comparing Unstructured Adaptive Mesh Solutions for the High Lift Common Research Model Airfoil,” *AIAA Journal*, Vol. 59, No. 9, 2021, pp. 3566–3584. doi:10.2514/1.J060088.

- [45] Park, M. A., Balan, A., Clerici, F., Alauzet, F., Loseille, A., Kamenetskiy, D. S., Krakos, J. A., Michal, T., and Galbraith, M. C., “Verification of Viscous Goal-Based Anisotropic Mesh Adaptation,” AIAA Paper 2021-1362, 2021. doi:10.2514/6.2021-1362.
- [46] Alauzet, F., and Frazza, L., “Feature-Based and Goal-Oriented Anisotropic Mesh Adaptation for RANS Applications in Aeronautics and Aerospace,” *Journal of Computational Physics*, Vol. 439, 2021, p. 110340. doi:10.1016/j.jcp.2021.110340.
- [47] Kamenetskiy, D. S., Krakos, J. A., Michal, T., Clerici, F., Alauzet, F., Loseille, A., Park, M. A., Wood, S., Balan, A., and Galbraith, M. C., “Anisotropic Goal-Based Mesh Adaptation Metric Clarification and Development,” AIAA Paper 2022-1245, 2022. doi:10.2514/6.2022-1245.
- [48] Michal, T., Kamenetskiy, D., and Krakos, J., “Anisotropic Adaptive Mesh Results for the Third High Lift Prediction Workshop (HiLiftPW-3),” AIAA Paper 2018-1257, 2018. doi:10.2514/6.2018-1257.
- [49] Park, M. A., Kleb, B., Anderson, W. K., Wood, S. L., Balan, A., Zhou, B. Y., and Gauger, N. R., “Exploring Unstructured Mesh Adaptation for Hybrid Reynolds-Averaged Navier-Stokes/Large Eddy Simulation,” AIAA Paper 2020-1139, 2020. doi:10.2514/6.2020-1139.
- [50] Alauzet, F., and Frazza, L., “3D RANS Anisotropic Mesh Adaptation on the High-Lift Version of NASA’s Common Research Model (HL-CRM),” AIAA Paper 2019-2947, 2019. doi:10.2514/6.2019-2947.
- [51] Alauzet, F., Clerici, F., Loseille, A., Morisco, C. T., and Vanharen, J., “Some progress on CFD high lift prediction using metric-based anisotropic mesh adaptation,” AIAA Paper 2022-388, 2022. doi:10.2514/6.2022-0388.
- [52] Sukas, H., and Sahin, M., “HEMLAB Algorithm Applied to the High-Lift JAXA Standard Model,” AIAA Paper 2021-1994, 2021. doi:10.2514/6.2021-1994.
- [53] Tsolakis, C., Chrisochoides, N., Park, M. A., Loseille, A., and Michal, T., “Parallel Anisotropic Unstructured Grid Adaptation,” *AIAA Journal*, Vol. 59, No. 11, 2021, pp. 4764–4776. doi:10.2514/1.J060270.
- [54] Park, M. A., Kleb, B., Jones, W. T., Krakos, J. A., Michal, T., Loseille, A., Haimes, R., and Dannenhoffer, J. F., III, “Geometry Modeling for Unstructured Mesh Adaptation,” AIAA Paper 2019-2946, 2019. doi:10.2514/6.2019-2946.
- [55] Park, M. A., Haimes, R., Wyman, N. J., Baker, P. A., and Loseille, A., “Boundary Representation Tolerance Impacts on Mesh Generation and Adaptation,” Tech. Rep. 2021-2992, 2021. doi:10.2514/6.2021-2992.
- [56] Taylor, N. J., and Gammon, M., “A Wind Tunnel Model of the NASA High Lift Common Research Model: A Geometry-Handling Perspective,” AIAA Paper 2019-3460, 2019. doi:10.2514/6.2019-3460.
- [57] Menier, V., Loseille, A., and Alauzet, F., “CFD Validation and Adaptivity for Viscous Flow Simulations,” AIAA Paper 2014-2925, 2014. doi:10.2514/6.2014-2925.
- [58] Biedron, R. T., Carlson, J.-R., Derlaga, J. M., Gnoffo, P. A., Hammond, D. P., Jacobson, K. E., Jones, W. T., Kleb, B., Lee-Rausch, E. M., Nielsen, E. J., Park, M. A., Rumsey, C. L., Thomas, J. L., Thompson, K. B., Waldon, A. C., Wang, L., and Wood, W. A., “FUN3D Manual: 13.7,” NASA TM-20205010139, Langley Research Center, Nov. 2020. doi:10.2514/6.20205010139.
- [59] Anderson, W. K., and Bonhaus, D. L., “An Implicit Upwind Algorithm for Computing Turbulent Flows on Unstructured Grids,” *Computers and Fluids*, Vol. 23, No. 1, 1994, pp. 1–22. doi:10.1016/0045-7930(94)90023-X.
- [60] Anderson, W. K., Newman, J. C., and Karman, S. L., “Stabilized Finite Elements in FUN3D,” *Journal of Aircraft*, Vol. 55, No. 2, 2018, pp. 696–714. doi:10.2514/1.C034482.
- [61] Akkurt, S., and Sahin, M., “An Efficient Edge Based Data Structure for the Compressible Reynolds-Averaged Navier-Stokes Equations on Hybrid Unstructured Meshes,” *International Journal for Numerical Methods in Fluids*, Vol. 94, No. 1, 2022, pp. 13–31. doi:10.1002/fld.5045.
- [62] Galbraith, M. C., Allmaras, S. R., and Darmofal, D. L., “SANS RANS Solutions for 3D Benchmark Configurations,” AIAA Paper 2018-1570, 2018. doi:10.2514/6.2018-1570.
- [63] Glasby, R. S., Erwin, J. T., Stefanski, D. L., Allmaras, S. R., Galbraith, M. C., Anderson, W. K., and Nichols, R. H., “Introduction to COFFE: The Next-Generation HPCMP CREATE™ -AV CFD Solver,” AIAA Paper 2016-567, 2016. doi:10.2514/6.2016-0567.
- [64] Holst, K. R., Glasby, R. S., and Erwin, J. T., “Current Status of the Finite-Element Fluid Solver (COFFE) within HPCMP CREATE™ -AV Kestrel,” AIAA Paper 2022-24, 2022. doi:10.2514/6.2022-0024.



- [65] Galbraith, M. C., “HLPW-4/GMGW-3: High Order Discretization Technology Focus Group Workshop Summary,” Reston, VA (submitted for publication).
- [66] Loseille, A., and Löhner, R., “Cavity-Based Operators for Mesh Adaptation,” AIAA Paper 2013–152, 2013. doi:10.2514/6.2013-152.
- [67] Loseille, A., Alauzet, F., and Menier, V., “Unique Cavity-Based Operator and Hierarchical Domain Partitioning for Fast Parallel Generation of Anisotropic Meshes,” *Computer-Aided Design*, Vol. 85, 2017, pp. 53–67. doi:10.1016/j.cad.2016.09.008, 24th International Meshing Roundtable Special Issue: Advances in Mesh Generation.
- [68] Loseille, A., “Unstructured Mesh Generation and Adaptation,” *Handbook of Numerical Methods for Hyperbolic Problems: Applied and Modern Issues*, Handbook of Numerical Analysis, Vol. 18, edited by R. Abgrall and C.-W. Shu, Elsevier, 2017, pp. 263–302. doi:10.1016/bs.hna.2016.10.004.
- [69] Park, M. A., “Anisotropic Output-Based Adaptation with Tetrahedral Cut Cells for Compressible Flows,” Ph.D. thesis, Massachusetts Institute of Technology, Sep. 2008. doi:1721.1/46363.
- [70] Haimes, R., and Drela, M., “On The Construction of Aircraft Conceptual Geometry for High-Fidelity Analysis and Design,” AIAA Paper 2012–683, 2012. doi:10.2514/6.2012-683.
- [71] Haimes, R., and Dannenhoffer, J. F., III, “EGADSLite: A Lightweight Geometry Kernel for HPC,” AIAA Paper 2018–1401, 2018. doi:10.2514/6.2018-1401.
- [72] Michal, T., and Krakos, J., “Anisotropic Mesh Adaptation Through Edge Primitive Operations,” AIAA Paper 2012–159, 2012. doi:10.2514/6.2012-159.
- [73] Carson, H. A., Huang, A. C., Galbraith, M. C., Allmaras, S. R., and Darmofal, D. L., “Mesh Optimization via Error Sampling and Synthesis: An Update,” AIAA Paper 2020–87, 2020. doi:10.2514/6.2020-0087.
- [74] Rumsey, C. L., Smith, B. R., and Huang, G. P., “Description of a Website Resource for Turbulence Modeling Verification and Validation,” AIAA Paper 2010–4742, 2010. doi:10.2514/6.2010-4742.
- [75] Rumsey, C. L., “Recent Developments on the Turbulence Modeling Resource Website,” AIAA Paper 2015–2927, 2015. doi:10.2514/6.2015-2927.
- [76] Ursachi, C.-I., Galbraith, M. C., Allmaras, S. R., and Darmofal, D. L., “Output-Based Adaptive Reynolds-Averaged Navier–Stokes Higher-Order Finite Element Solutions on a Multielement Airfoil,” *AIAA Journal*, Vol. 59, No. 7, 2021, pp. 2532–2545. doi:10.2514/1.J059968.
- [77] Moss, B. R., Bagheri, A. K., and Da Ronch, A., “Effect of Mesh Characteristics on the Flow Solutions around a Multi–element Airfoil using SU2,” AIAA Paper 2020–3218, 2020. doi:10.2514/6.2020-3218.
- [78] Chuen, A. M., and Chan, W. M., “Mesh Effects on Flow Solutions for a 2-D Multi-Element Airfoil Using Structured Overset Methods,” AIAA Paper 2020–3222, 2020. doi:10.2514/6.2020-3222.
- [79] Masters, J. S., Lynch, C. E., and Glasby, R. S., “Kestrel Results on a 2D Cut of the High Lift Common Research Model Wing,” AIAA Paper 2021–942, 2021. doi:10.2514/6.2021-0942.
- [80] Galbraith, M. C., Ursachi, C.-I., Chandel, D., Allmaras, S. R., Darmofal, D. L., Glasby, R. S., Stefanski, D. L., Erwin, J. T., Holst, K. R., Hereth, E. A., Mukhopadhyaya, J., and Alonso, J. J., “Comparisons of HPCMP CREATE™-AV Kestrel-COFFE, SU2, and MIT SANS RANS Solutions using Output-Based Adapted Meshes for a Multi-Element Airfoil,” AIAA Paper 2021–1080, 2021. doi:10.2514/6.2021-1080.
- [81] de Souza, R. F., Ferrari, M. A., and Ferrari, D. B., “Mesh Effects for 2-D CFD Solutions on a High-Lift CRM Wing Section,” AIAA Paper 2021–1361, 2021. doi:10.2514/6.2021-1361.
- [82] Gammon, M., Bucklow, H., and Fairey, R., “A Review of Common Geometry Issues Affecting Mesh Generation,” AIAA Paper 2018–1402, 2018. doi:10.2514/6.2018-1402.
- [83] Rumsey, C. L., “The NASA Juncture Flow Test as a Model for Effective CFD/Experimental Collaboration,” AIAA Paper 2018–3319, 2018. doi:10.2514/6.2018-3319.
- [84] Schumann, J.-E., Toosi, S., and Larsson, J., “Assessment of Grid Anisotropy Effects on Large-Eddy-Simulation Models with Different Length Scales,” *AIAA Journal*, Vol. 58, No. 10, 2020, pp. 4522–4533. doi:10.2514/1.J058498.